AURORAL THERMOSPHERIC TEMPERATURES

A

THESIS

Presented to the Faculty of the

University of Alaska in partial fulfillment

of the Requirements

for the Degree of

MASTER OF SCIENCE

By

Marjorie Althea Cole, A. B.

Fairbanks, Alaska

December 1980

AURORAL THERMOSPHERIC TEMPERATURES

RECOMMENDED:

Gerald J. Romick

Chairman, Advisory Committee

Program Head

Director

APPROVED:

Dean of the College of Environmental Sciences

12-4-80

Date

Vice Chancellor for Research and Advanced Study

12/6/80

Date

ABSTRACT

A pressure-scanning Fabry-Perot interferometer was used to determine thermospheric, neutral temperature by measuring the Doppler width of the oxygen red line in the auroral spectrum.

A technique for analyzing the interferometric measurements using supplemental photometric data and an atmospheric model is developed to infer the kinetic neutral temperature of the atmosphere at the mean altitude of the auroral emission. Observed relationships with ion and electron temperature data from incoherent scatter radar are investigated in terms of energy input and ionic composition.

A four-hour delay between geomagnetic activity and increase in the neutral temperature is suggested. The neutral thermospheric temperature is cooler than predicted by the assumed atmospheric model. The temperature of the polar atmosphere is shown to be more dependent on geomagnetic activity, over a two-day period, than is predicted by the Jacchia (1971) model atmosphere.

ACKNOWLEDGMENTS

My thanks to Drs. M. H. Rees, G. J. Romick, G. G. Sivjee, R. Parthasarathy, L. C. Hoskins, and G. R. Swenson (Marshall Space Flight Center) for their guidance throughout the study. In addition, I thank D. L. Osborne, Dr. T. J. Hallinan, and S. C. MacInnes for their help and patience during the project. Dr. V. B. Wickwar and M. A. McCready (SRI International) supplied the radar data. The Fabry-Perot interferometer was made available through a cooperative study with the Marshall Space Flight Center.

I am appreciative of all my friends at the Geophysical Institute and in Alaska who made my years at the University of Alaska enjoyable. And I thank the aurora for being beautiful.

The research was supported by the National Science Foundation, grant #ATM77-23141.

Lo, here a new Aurora,
  Nay one of a different form.
It tantalizes our imagination
  Then with the night is gone.

CONTENTS

LIST OF FIGURES

LIST OF TABLES

STATEMENT BY AUTHOR

This thesis has been submitted in partial fulfillment of requirements for an advanced degree at The University of Alaska and is deposited in the University Library to be made available to borrowers under rules of the Library.

Brief quotations from this thesis are allowable without special permission, provided that accurate acknowledgement of source is made. Requests for permission for extended quotation from or reproduction of material contained in this manuscript may be granted by the head of the major department or the Dean of the Graduate College when in his judgement the proposed use of the material is in the interests of scholarship. In all other instances, however, permission must be obtained from the author.

SIGNED: Marjorie A Cole

I. INTRODUCTION

There has been considerable discussion and sporadic observations of the neutral temperature associated with the auroral thermosphere.

Since Babcock's first measurements (Babcock, 1923) it has been realized that the kinetic temperature of the upper atmosphere could be deduced optically by measuring the Doppler broadening of emission lines in the airglow and aurora. His original work succeeded in placing an upper limit on the observed atmospheric temperature (Nilson and Shepherd, 1961). Recent technological advancements have improved both spectral and temporal resolution of Doppler line widths of several forbidden emissions occurring in the aurora and airglow. Generally, the red and green lines of atomic oxygen are used to determine the neutral temperature in the atmosphere.

Because of its good light gathering capability and its high resolution, the Fabry-Perot interferometer (FPI) is well suited for determining spectral line widths (Roble, 1969). A pressure-scanning FPI has been used to carry out observations of the midlatitude neutral temperature at the Fritz Peak Observatory since 1972. The results (summarized by Hernandez and Roble, 1979) indicate that high latitude auroral heating may be important in determining global,

high altitude, atmospheric, thermal characteristics. At the Mawson Institute for Antarctic Research, observations show a greater neutral temperature dependence on geomagnetic activity than was predicted by the atmospheric model of Jacchia (Jacka et al., 1979). Diurnal variations in neutral temperature have been measured for entire 24-hour periods (Cocks and Jacka, 1979) by placing a high resolution FPI in series with a smaller low resolution FPI which isolates the emission from the background continuum.

The above investigators deal primarily with observations of the airglow. Sporadic observations of the neutral temperature in auroral regions include the work of Kamiyama and Okano which shows the temperature varying from 550^{o} to 1150^{o}K in the 200km region (unpublished results, 1977). Observations were also conducted by the University of Michigan (Hays et al., 1979). Most of the conclusions of the Michigan study relate to thermospheric winds although it was also shown that the neutral temperature may be different than was expected. However, the observed neutral temperature is a function of the altitude of the radiating species and, during auroral activity, the altitude is dependent on the characteristic energy of the precipitating particles. Because of the problem in determining altitude of the emission, there was uncertainty in interpreting the observed temperature.

The auroral neutral atmosphere is heated primarily by

particle flux and electric fields. The heating results in vertical convection at high latitudes (Hays et al., 1973) in addition to possible increases in atmospheric temperature. The former drives a global circulation which has been experimentally observed (Knudson et al., 1977, Richmond, 1979, and Hays and Roble, 1971a). Observation of the latter requires measurement of ion, electron, and neutral temperatures.

Rocket experiments give measurements of atmospheric temperatures but are of short duration. Ion and electron temperatures inferred from radar measurements indicate atmospheric warming of ions and electrons following auroral events (Kelly, 1979). Ground-based studies can be used to determine neutral and ion temperatures.

In a cooperative program between Marshall Space Flight Center and the Geophysical Institute at the University of Alaska, a high resolution FPI is used to study the thermal characteristics of the high latitude neutral atmosphere by measuring the Doppler broadening of the atomic oxygen red line in the auroral spectrum. Observations are carried out at the Poker Flat Research Rocket Range located north of the Geophysical Institute at 65 degrees geomagnetic latitude in a region of high auroral activity. The availability of supplemental data is important in the analysis of the temperature measurements. These include the intensity of several auroral emission features recorded by meridian

scanning photometers, ion and electron temperature data, and electric field observations measured by the Thomson scatter radar at Chatanika.

After describing the installation of the FPI system, this thesis examines whether the variations in neutral temperature observed with the FPI indicate real temperature changes or whether the variations are due primarily to the change in the mean altitude of emission. Discussion then focuses on the thermal behavior of the neutral atmosphere during auroral activity.

II. EXPERIMENTAL APPROACH

Line Profiles

The heating and dynamics of the neutral atmosphere can be monitored by observing changes in the spectral profiles of an optical emission. The changes, resulting from the relative motion between the radiating atom and the observer, give rise to an apparent shift in the wavelength of the observed emission line. This shift, known as the Doppler effect, is used in Chapter VIII to determine the line of sight velocity (or wind) of the radiating species.

If the radiating species is in local thermal equilibrium and the orientation of thermal motion is random, the Doppler shift produces an apparent broadening in the observed spectral line. Mathematically, the Maxwellian distribution of velocities is convolved with a sharp Lorentzian profile approximated by a Delta function, representing the spectral emission, to produce a Gaussian profile.

$$\text{Doppler profile} = D(\lambda) = \frac{1}{\delta\lambda_D\sqrt{\pi}} \exp\left(\frac{-\delta\lambda^2}{\delta\lambda_D^2}\right) \qquad (1)$$

where $\delta\lambda = \lambda - \lambda_0$

λ_0 = reference wavelength

λ = observed wavelength

$\delta\lambda_D = \lambda_0 v_0 / c$

$v_0 = \sqrt{\frac{2kT}{M}}$

C = velocity of light

k = Boltzman constant

M = mass of radiating species

T = kinetic temperature

$$\text{Doppler width} = \Delta\lambda_D = \frac{2\lambda_0}{c}\sqrt{\frac{2kT\ln 2}{M}} \qquad (2)$$

The Doppler width of the profile is most pronounced for atoms with a small mass and a high kinetic temperature.

In addition to the thermal broadening, pressure broadening will occur. Elastic collisions between the atoms during emission interrupt the train of radiation and introduce smaller sinusoidal wave trains. These remain constant until the next collision occurs. The net effect of the elastic collisions produces a Lorentzian profile.

$$\text{Lorentz profile} = L(\nu) = \frac{\Delta\nu}{\pi}\,\frac{1}{\Delta\nu^2 + \delta\nu^2} \qquad (3)$$

where $\delta\nu = \nu_0 - \nu$

ν_0 = reference frequency

ν = observed frequency

$\Delta\nu$ = collision frequency

When both thermal and collisional broadening are significant, the resulting profile (known as the Voigt profile) is the product of the Doppler and Lorentz profiles. Thermal motions dominate the shape of the Voigt profile near the central frequency. Collisional dependence dominates in the wings (Shore and Mentzel, 1968).

In general, the relative importance of the profiles is dependent primarily on the kinetic temperature and density of the radiating atoms. In the thermosphere the effects due

to thermal motion is significantly more important than collisional effects in determining the width of the Voigt profile. Hence Lorentz broadening will be ignored.

The Experiment

The high resolution Fabry-Perot interferometer (FPI) is routinely used to measure line widths of emissions occurring in the auroral spectrum. The two most frequently observed emissions are two of the brightest in the aurora. Specifically, they originate from the forbidden transitions of oxygen 5577A $O(^1S) \rightarrow O(^1D)$ and 6300A $O(^1D) \rightarrow O(^3P)$. The natural line widths of these emissions are small (on the order of 10^{-11} and 10^{-13}A) because of their long radiative lifetimes (0.74sec and 110sec, Chamberlain, 1961). These emissions occur near 110km and 200km, respectively, allowing the study of two different altitude regimes in the terrestrial atmosphere.

In this thesis, the neutral temperature is determined only for the 6300A emission line of the aurora. The Fabry-Perot interferometer observing this emission has an etalon with reflective coatings that are maximized for best resolution at 6300A. The primary production mechanism for $O(^1D)$ is through electron impact excitation of the oxygen atom (Vallance-Jones, 1974) so that the radiating atom can be assumed in thermal equilibrium with the surrounding neutral atmosphere.

III. INSTRUMENTATION

General Description

The concentric rings comprising an interferometric fringe contain information about the kinetic temperature of the radiating atoms. Usually temperature information is determined by measuring the line width of the fringe profile using static imaging techniques or by pressure scanning (described later).

The basic principles describing the Fabry-Perot interferometer are given in many optical textbooks (eg. Nussbaum and Phillips, 1976 and Born and Wolf, 1959). In brief, an incident electromagnetic signal is multiply reflected and partially transmitted by the semireflecting surfaces of the etalon (Figure 1a). The optical path difference between the transmitted beams leads to either constructive or destructive interference. If a monochromatic laser line is used as the signal source, the resulting multiple beam interfence is characterized by the Airy function (Figure 1b).

$$\text{Airy function} = F_1(\chi) = \frac{1}{2\pi} \frac{1}{1 - 2R\cos\chi + R^2} \qquad (4)$$

$$\text{Airy width} = \Delta\lambda_1 = \Delta\sigma\,(1-R)/\pi R^{1/2} \qquad (5)$$

where R = etalon reflectivity

$\Delta\sigma$ = free spectral range

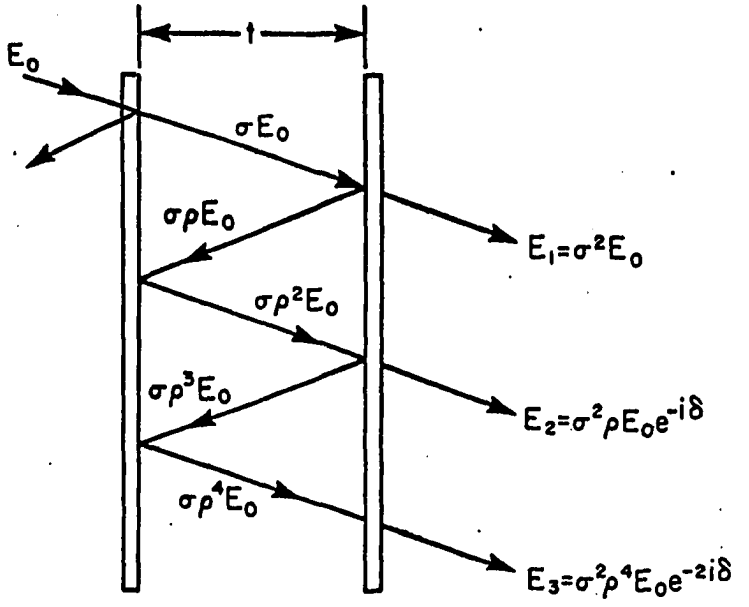

$$E_T=\sigma^2E_0\left\{1+\rho^2e^{-i\delta}+\rho^4e^{-i2\delta}+\ldots+\rho^{2N-2}e^{-(N-1)\delta}\right\}=\frac{\sigma^2E_0}{1-\rho^2e^{-i\delta}}$$

a. Multiple reflections: E_o = incident electric wave, ρ = reflection coefficient, σ = transmission coefficient, δ = phase difference, t = plate spacing, E_T = transmitted wave.

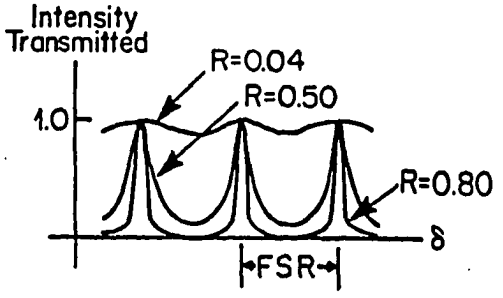

$$I_T=\tfrac{1}{2}E_TE_T^*=\frac{1}{2\pi}\,\frac{1}{1-2R\cos X+R^2}$$

b. Throughput: I_T = transmitted intensity, FSR = free spectral range = observed wavelength region.

Figure 1. Basic principles of the Fabry-Perot interferometer (Source: Nussbaum and Phillips, 1976).

where $\chi = \delta - \delta_o$ (6)

δ_o = phase difference between consecutive beams of reference signal

δ = phase difference of observed signal

The width of the Airy function is primarily dependent on reflectivity and spacing of the plate.

The FPI used for the observations in this thesis (Figure 2) is provided by the Marshall Space Flight Center through the courtesy of Dr. G. R. Swenson as part of a cooperative research project with the Geophysical Institute. A periscope is used to select the elevation and azimuth for observation. Incident light is directed into an airtight etalon chamber and through the Fabry-Perot etalon. The central image of the resulting interference fringe is then focused on the 1mm diameter photocathode of a photomultiplier tube chosen for its very low dark current. The 6300A signal is isolated from the surrounding continuum of light and from multiple orders of other spectral emissions by a narrow bandpass 6300A filter. A controlled influx of gas into the etalon chamber changes the index of refraction and hence the optical path length between the etalon plates. The system records the intensity of the central image for at least one free spectral range of .198A (Figure 1).

The electronics operating the FPI are shown in Figure 3.

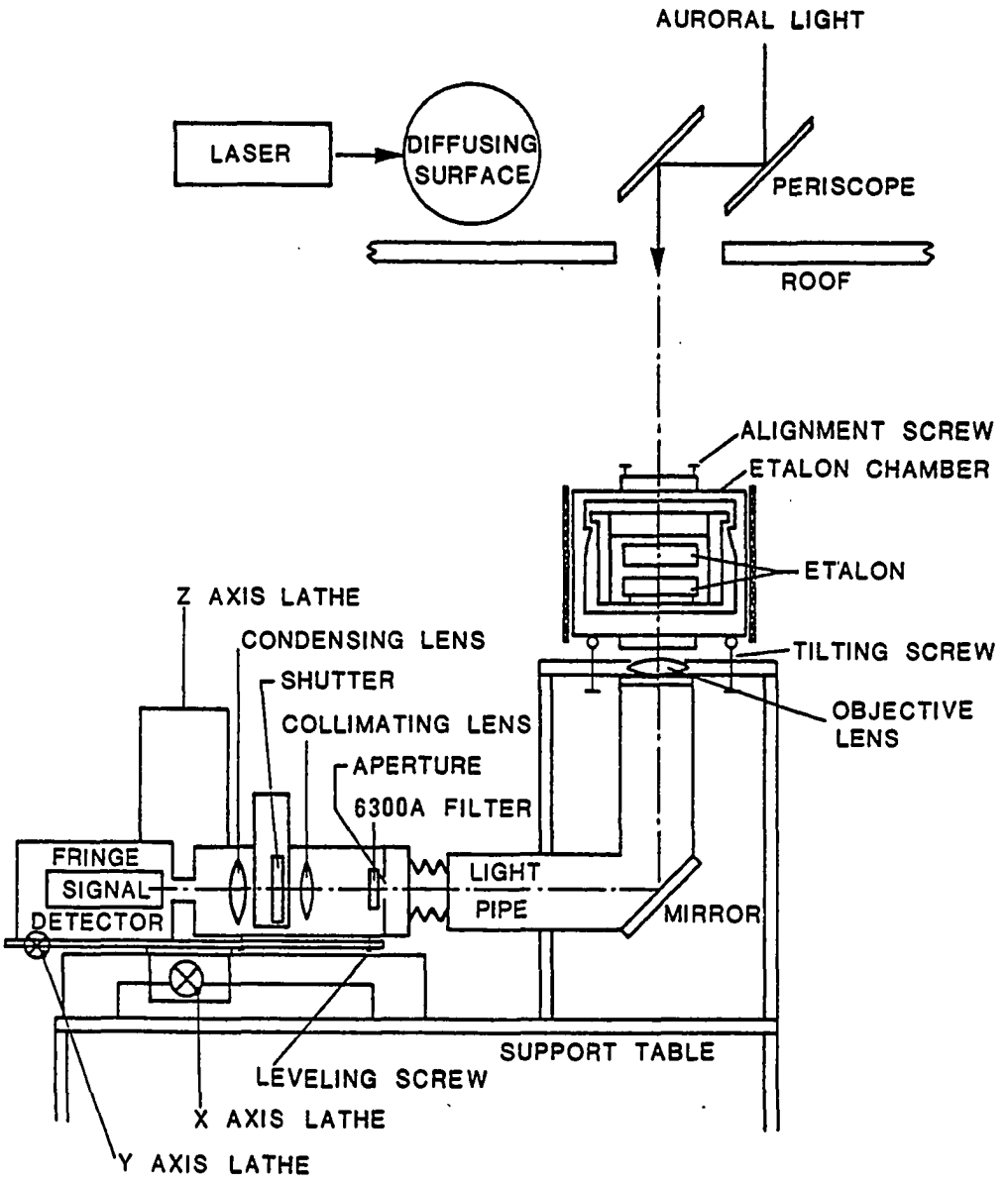

Figure 2. Fabry-Perot interferometer with optical support.

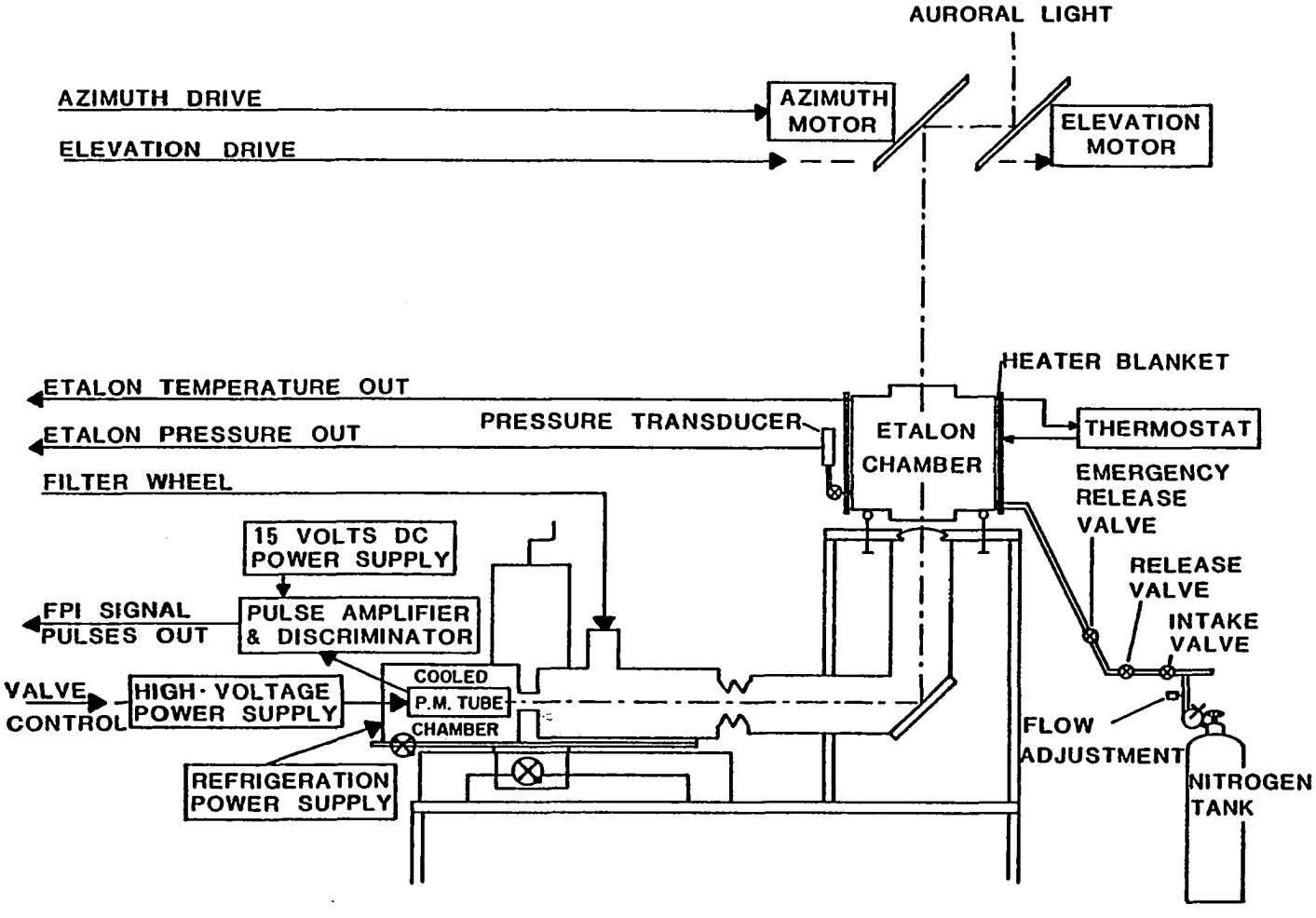

Figure 3. Signal detection devices and electrical support.

During a pressure scan, the output parameters of the system are the etalon temperature, the etalon pressure, and the signal intensity of the central image. These are measured by a thermocouple, a pressure transducer (strain gauge), and a cooled photomultiplier tube.

A pressure scan is initiated by opening the intake valve and closing the release valve. Compressed gas flows from a nitrogen tank into the etalon chamber. The pressure within the chamber increases so that a change in the index of refraction (and hence in optical path length) between the plates varies the wavelength of the central image. The rate of flow from the tank is controlled by the valves on the nitrogen tank and by a more sensitive flow-adjustment system.

When the pressure within the chamber reaches a preset maximum, the intake valve closes and the release valve opens. The chamber vents until the preset minimum pressure is attained and a new pressure scan begins.

The sudden changes in pressure cause the temperature of the gas in the etalon to vary. The usable portion of the profile begins after the temperature has stabilized. Both the rate and length of the pressure scan can be varied. Selection of these depends mainly on the intensity of the aurora. An emergency release valve, set for 5psi above atmospheric pressure, prevents possible damage to the etalon.

As the pressure in the chamber is varied, the intensity

of the central image is measured by the photomultiplier tube. The number of pulses from the photomultiplier is linearly related to the brightness of the central image and hence the intensity of light of a given wavelength. Pulses from the photomultiplier tube are sent through a discriminator to a pulse amplifier. (Cooling of the photomultiplier tube reduces spontaneous emission of electrons from the photocathode, hence reducing the dark count. Because of the cooling, condensation within the photomultiplier housing was a recurrent problem and an aggravating source of electrical noise.)

Pulses from the photomultiplier above a minimum voltage were counted by a scaler-timer, converted to an analog mode by a digital-to-analog converter, and plotted against the pressure output on an X-Y chart recorder. This produced the fringe profile in analog. However, storage of the digital output for subsequent analysis was desirable. The method developed for recording the data is discussed in the next section.

Recording of Data

An existing Meridian Scanning Photometer system (MSP) is located at the same optics site (Romick, 1976) where the FPI is operated and stores digital data on magnetic tape. The recording format allows room for data sources other than the MSP itself. Data from the FPI were made compatible with the MSP data format by the addition of an appropriate

MSP/FPI interface (Appendix). The present system for recording the FPI data is based on the 4 second data scans determined by the MSP. The system is shown in Figure 4.

The MSP system monitors the intensity of several emissions in the auroral spectrum along the meridian. The observed emissions are: 6300A $O(^1D)$, 5577A $O(^1S)$, 4861A H_β, and 4278A N_2^+1NG(0,1). Auroral intensities vary greatly and concurrent operation of the two systems assures that photometric MSP data are available for the data analysis. Specifically, the photometric intensity of 6300A for the observation angle of the interferometer is used to normalize the FPI signal. It is an advantage to have the FPI data on the same magnetic tape as the normalization signal so that only one software program is necessary to extract the information pertinent to the FPI.

Analog-to-digital voltmeters convert the etalon temperature and pressure voltages to digital format. The output (in binary coded decimal) is continually updated so the current information is gated into the interface with the appropriate address code and option from the MSP software. Analog output of the etalon temperature and pressure are monitored frequently on the strip and X-Y chart recorders, respectively. Sample output appears in Figure 5a. Pulses from the photomultiplier are counted in the interface.

The azimuth and elevation of the observation are set manually by remote control from the periscope control panel.

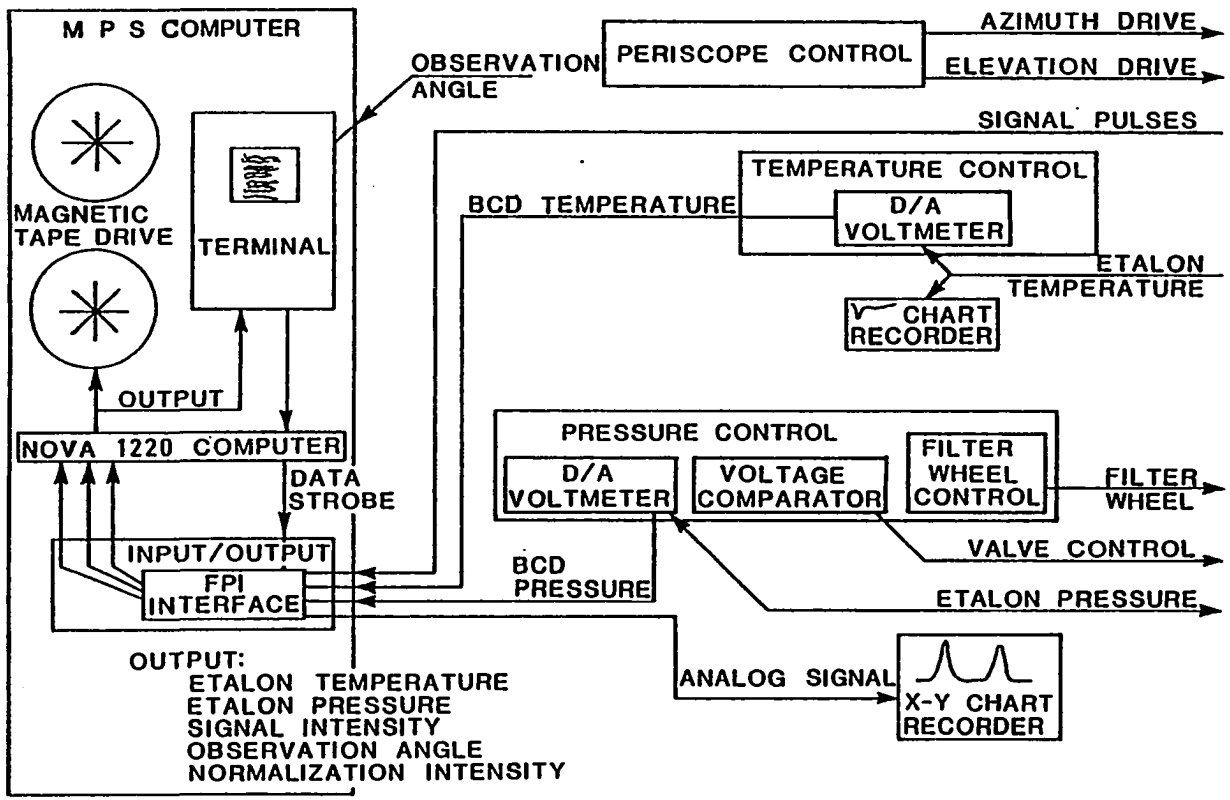

Figure 4. Control panels and computer system.

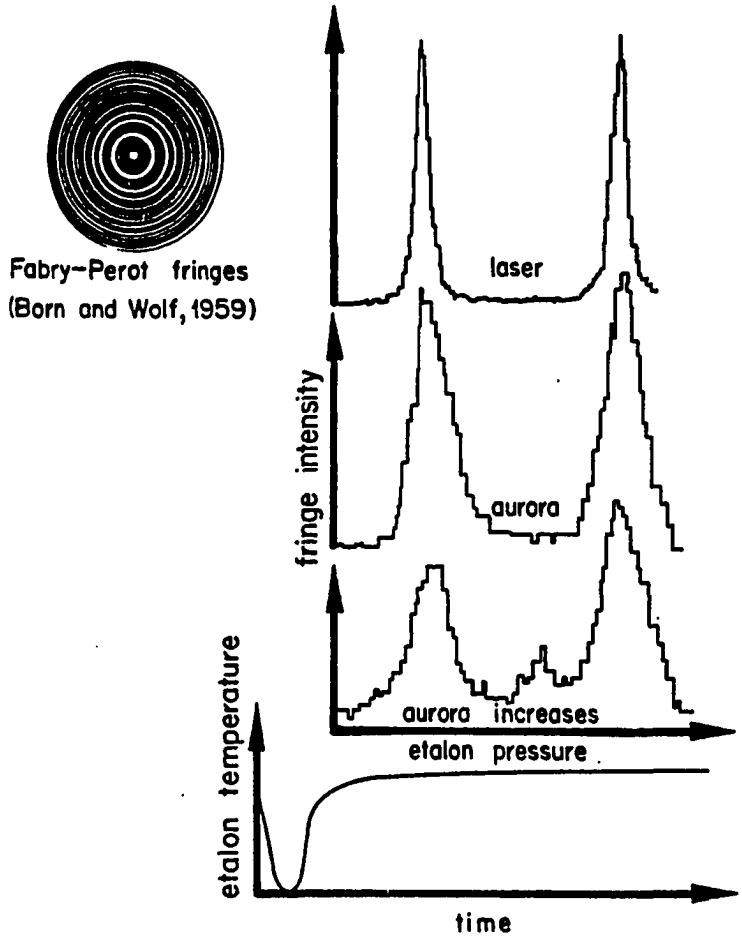

a. Analog output.

```
592  798   26  103
PF   5577  4278  4861  6300  52/12:44:42   N=1
103  7200  2393    35   474

592  825   64  103
PF   5577  4278  4861  6300  52/12:44:50   N=1
103  7830  4030    35   391

592  827  112  103
PF   5577  4278  4861  6300  52/12:44:50   N=1
103  8370  3770    42   549
```

b. Digital output.

Figure 5. Fabry-Perot interference fringe with real-time sample output.

The angle of observation is keyed into the computer.

The MSP data acquisition program requests the FPI data (by means of the appropriate device code) once each 4 second scan. The data strobe temporarily prohibits further input to the interface. Temperature, pressure, and signal count are read into the memory. When the count is read by the MSP software, it is simultaneously directed through a digital-to-analog converter (located in the interface) to the X-Y chart recorder. The counter is reset and the interface then resumes normal operation. The software places the FPI data (etalon temperature, etalon pressure, signal count, and observation angle) in the first 4 memory locations of each MSP data set. The data are recorded on magnetic tape. Sample output is shown in Figure 5b.

The Interferometer

Design specifications for the FPI are listed in Table 1. Extra-pure dry nitrogen, item 11, is used as the scanning gas since condensation within the chamber is undesirable. The filter's transmission characteristics, item 12, are determined using a quartz-halogen lamp and facilities at the Geophysical Institute. The overall instrument finesse, item 5, is verified experimentally.

Defects in the etalon plates broaden the instrumental profile. The amount that each defect broadens the profiles ($\Delta\lambda_i$) is characterized by a defect finesse ($N_i = FSR/\Delta\lambda_i$). If each defect finesse is assumed Gaussian (so that the

1.	Etalon plates	
	effective diameter	13.3 cm
	flatness	λ /180
	roughness defect, N_2	38.4
	reflective coatings	five alternate layers of AnS and cryolite
	reflectivity	0.85 at 6300A
	reflective finesse, N_1	19.3 at 6300A
	spherical defect finesse, N_3	20.3
	sagittal	1.55(-4)cm
	spacing	1cm
2.	Objective lens	
	diameter	15.24cm
	focal length	121.9cm
3.	Aperture	
	diameter	0.436cm
	finesse, N_4	19.6
4.	Instrumental field of view	0.2°
5.	Over-all instrument finesse, N_T	11 at 6300A
6.	Photomultiplier	FW130
	photocathode	s-20
	effective aperture	0.254cm
	dark count (cooled to -10°C)	1-2counts/sec
7.	Pressure change for one order	0.117atm
8.	Resolving power	350,000
9.	Operating order	31,700
10.	Free spectral range	0.198A
11.	Scanning gas	dry nitrogen
12.	Interference filter I	
	diameter	5.4cm
	half width	20A
	peak transmission	60%
	peak wavelength	6308A
	Interference filter II	
	diameter	5.4cm
	half-width	5A
	peak transmission	65%
	peak wavelength	6301A

Table 1. Specifications for the Fabry-Perot interferometer.

squares of the widths are additive), the total finesse (N_T) will be:

$$\frac{1}{N_T^2} = \sum_i \frac{1}{N_i^2} \tag{7}$$

Experimentally the total finesse is determined by measuring the line width (and hence instrumental broadening) with respect to the FSR using a helium-neon laser as a signal source. The laser is a monochromatic light source with a wavelength (6328A) near that of $O(^1D)$. Since the finesse is dependent on the reflectivity (and hence wavelength), the 6328A line of the laser is convenient for determining the interferometer's finesse near 6300A. The width of the laser beam is negligible so that the measured width of the profile is assumed to be due entirely to instrumental broadening. The finesse ($N_T = FSR/\Delta\lambda_T$) is a unitless ratio and is calculated directly from the width of the profile and the separation of the consecutive fringes. The resolution of the instrument can then be determined ($R = FSR/N_T$).

Careful alignment of the interferometer produces a total finesse nearly equal to the value derived from the parameters listed in Table 1. This indicates that the actual values of these parameters are close to their design specifications.

Alignment

The resolution of the interferometer is dependent on the degree to which the etalon plates are parallel and on the focus of the central image onto the photocathode.

Alignment of the plates can be maintained only if the temperature of the etalon itself remains constant. Thus, the etalon chamber is maintained in a thermally controlled environment by careful thermostatic control (+/- .2^{o}C) and insulation of the outside wall. It works well to have the room on the order of 5^{o}C cooler than the etalon heater. In this way the temperature of the etalon chamber is controlled by the heater even when the temperature of the room varies by several degrees.

Alignment of the plates is attempted only after the etalon has been maintained at its constant, operating temperature for at least one day.

To align the system, the light pipe (Figure 2) is separated so that a diffuse laser beam can be shone along the light path and through the etalon in the reverse of normal operation. The concentric rings, appearing at the top of the etalon, are adjusted by the adjustment screws so that the image is unchanged for all angles that the etalon is viewed. This assures that the plates are parallel. The adjustment is usually easiest if the central image is visible and the gas pressure within the etalon is held constant. The adjustment screws place pressure directly on the plates. (Caution: More than three or four turns is too much pressure for the plates and may warp or even fracture the etalon.)

Having adjusted the plates with a central image visible,

the detection system is reassembled and the laser is returned to its normal operating position. Alignment and focus of the central image of the FPI fringe is then accomplished by moving the detector system along the axes until the photomultiplier records the maximum signal.

For best resolution and maximum finesse, it is usually necessary to repeat the above procedures several times. A pressure scan of the diffused laser beam yields a profile consisting of two fringes from which the free spectral range and line broadening are measured. With luck and a little skill, the total finesse will be near 11 with an instrumental resolution of .018A.

The final step in the alignment is to tilt the 6300A filter for maximum transmission of the oxygen red line using the aurora itself as a signal source.

IV. DATA ACQUISITION

Data were collected for the nights shown in Table 2. Operation was primarily for two series of nights and varied from 4 to 16 hours. Data were recorded concurrently by the Chatanika Radar for UT days 052, 087, and 088, 1979. Meridian Scanning Photometer data exist for all times when the Fabry-Perot interferometer measurements were made except day 039.

A minimum of 100 points of data per free spectral range (peak to peak) is recorded requiring roughly 7½ minutes per profile. For each peak, both points at half height are included in the scan. Scanning time can be lengthened if the 6300A intensity is low. Recycle time is approximately 2½ minutes including the time necessary for the etalon temperature to stabilize.

The continual influx of expanding nitrogen gas may cause a small but gradual shift in the finesse. A profile of the laser is recorded at least once every six hours to check alignment and resolution of the interferometer. The laser beam is diffused and attenuated to an intensity on the order of an intense aurora. Adjustments in the values for the defect finesses in the analysis can accomodate minor variation in the instrument resolution. Major changes require realignment of the system.

Fabry-Perot Interferometer--Poker Flat

Spring 1979 Schedule

UT day	UT date	MSP	Radar	Comments
039	8 Feb	no	no	Clear, little activity
051	20 Feb	yes	no	Clear, little activity
052	21 Feb	yes	yes	Clear, active
053	22 Feb	yes	no	Clear
054	23 Feb	yes	no	Clear
056	25 Feb	yes	no	Clear
057	26 Feb	yes	yes	Poor resolution
074	15 Mar	no	yes	Clouds and snow
083	24 Mar	yes	no	70% transmission
085	26 Mar	yes	no	Became cloudy
087	28 Mar	yes	yes	Clearing
088	29 Mar	yes	yes	Some clouds
089	30 Mar	yes	yes	Cloudy, some signal
090	31 Mar	yes	no	Clearing
091	1 Apr	yes	no	Mostly clear
108	18 Apr	yes	yes	Extraneous noise

Table 2. Spring 1979 observing schedule.

Under cloudy conditions the composite signal seen by the interferometer originates from a variety of locations (due to scattering by the clouds) and is composed of a variety of Doppler shifts. The retrieved profile is broadened by the superposition of the profiles and an erroneously high temperature is deduced.

In cloudy weather, the intensities of the auroral emissions recorded by the MSP will also be attenuated. The most noticeable variation is in the 4278A intensity (frequently used in data analysis). Generally this emission is spatially well defined but the scattering by clouds smears its recorded intensity.

V. DATA REDUCTION

Equations

The first step in data reduction is to obtain the Fabry-Perot interferometric fringe. The data reduction algorithm then provides for a numerical, least squares matching of the experimental fringe patterns with a theoretical fringe profile. For mathematical ease in convolving the functions, both the experimental and theoretical profiles are transformed to frequency space. The method used here follows that of Hays and Roble (1971b).

A flow chart of the data reduction routine and sample output is shown in Figure 6. The index of refraction is proportional to the number-density of the gas between the etalon plates.

$$\text{density} \propto \text{index} - 1 \propto \frac{\text{pressure (PSI)}}{\text{temperature } (^{\circ}\text{K})} \qquad (8)$$

The fringe signal intensity is normalized with the overall signal intensity.

$$\text{signal} \propto \frac{\text{FPI signal count} - \text{FPI dark count}}{\text{MSP normalizing count} - \text{MSP dark count}} \qquad (9)$$

These equations are used to determine the experimental fringe profile and provide the input parameters for determining kinetic temperature.

The signal from the photomultiplier represents the sum

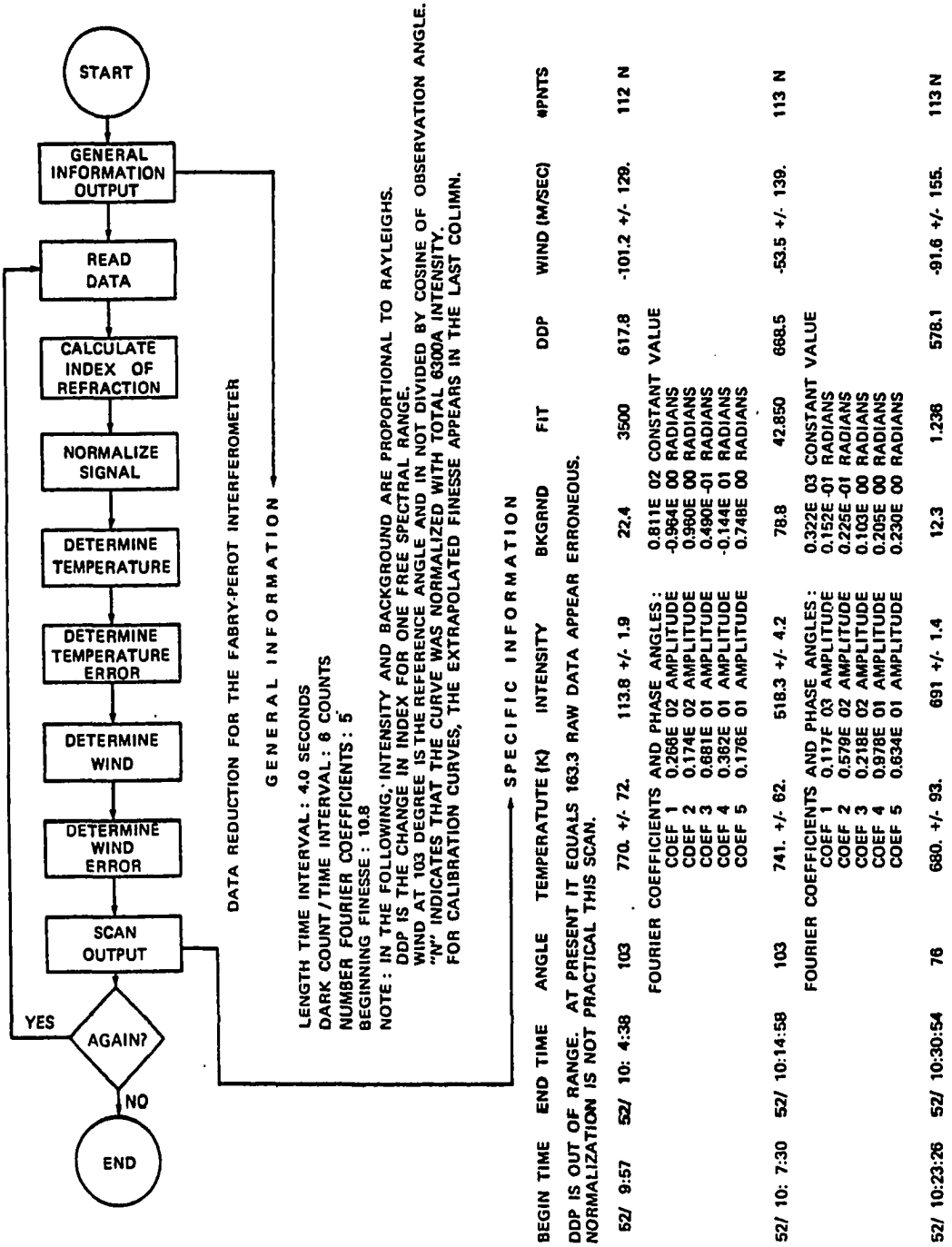

Figure 6. Flowchart of data analysis program with sample output.

of the optical signal and random noise. The latter may be filtered from the signal using standard frequency analysis techniques. By transforming to frequency space, the data are represented as a Fourier sum.

$$\text{Experimental profile} = \hat{Y}_E(\chi) = \frac{\hat{Y}_{co}}{2} + \sum_{m=1}^{\infty} \hat{Y}_m \cos\left[m(\chi+\alpha_m)\right] \quad (10)$$

where $\hat{Y}_m$ = Fourier coefficient = $(\hat{Y}_{cm}^2 + \hat{Y}_{sm}^2)^{1/2}$

α_m = Fourier phase angle = $\tan^{-1}(\hat{Y}_{cm}/\hat{Y}_{sm})$

$\hat{Y}_{sm}$, $\hat{Y}_{cm}$ = Fourier sine and cosine transforms

Y_E is an even function.

Since the signal information is limited by the 4 second integration period, the signal-to-noise ratio of the synthesized fringe is enhanced if only the first five or so coefficients are retained for the analysis.

The theoretical fringe is determined as the convolution of the instrumental and physical line broadening functions listed in Table 3. In frequency space, the total theoretical profile is represented as the sum of these functions.

Instrumental broadening includes the Airy function, discussed previously, as well as the broadening from the instrumental defects listed in Table 1. Broadening of the profile due to imperfections in the smoothness of the etalon plates is described by a Gaussian distribution assumed radially symmetric about the center of the etalon (Hays and

COORDINATE SPACE	FREQUENCY SPACE*
Instrumental broadening:	
1. $F_1(x)$ = Airy function	$[1+2\sum_{n=1}^{\infty} R^n \cos nx]$
2. $F_2(x)$ = Plate smoothness	$\sum_{n=1}^{\infty} \exp(-n g(N_2)^2)$
3. $F_3(x)$ = Spherical defect	$\sum_{n=1}^{\infty} \mathrm{sinc}(n g(N_3))$
4. $F_4(x)$ = Aperture defect	$\sum_{n=1}^{\infty} \mathrm{sinc}(n g(N_4))$
Physical broadening:	$g(N_i) = \frac{\pi}{(\ln 2)^{1/2} N_i}$
5. D(x) = Doppler profile	$\sum_{n=1}^{\infty} \exp\left(\frac{\pi \Delta\lambda_D}{FSR\,(\ln 2)^{1/2}}\right)$
6. L(x) = Lorentz profile	$\sum_{n=1}^{\infty} \exp(-Ln)$

*Constant coefficients not included

Table 3. Line broadening functions.

Roble, 1971b; after Chabbal, 1953). The width ($\Delta\lambda_2$) of this Gaussian function is characterized by the roughness defect finesse ($N_2 = FSR/\Delta\lambda_2$). Effects of the spherical defects of the etalon (Hays and Roble, 1971b; after Chabbal, 1953) and the finite size of the aperture (Hays and Roble, 1971b) are assumed to be represented by square broadening functions. Their widths are characterized by the spherical defect and aperture finesses, respectively.

Thermal and collisional broadening are represented by the Doppler and Lorentzian profiles. Both are included in an analysis by Ballik (1966). However, in the atmosphere at 200km, the 6300A emission of atomic oxygen at 700°K has a Doppler width of .03A while the Lorentzian width is much smaller. Hence Lorentzian broadening is ignored.

The final step in determining kinetic temperature is the least squares matching of the experimental (Y_E) and theoretical (Y_T) profiles in frequency space.

$$\text{Square difference} = \langle \delta Y^2 \rangle = \int_{-\Delta\chi/2}^{\Delta\chi/2} \left[Y_E(\chi) - Y_T(\chi) \right]^2 d\chi \qquad (11)$$

where $\Delta\chi$ = one free spectral range

Substitution of Y_E and Y_T yields:

$$\langle \delta Y^2 \rangle = \sum_{m=2}^{M} Y_m^2 - S_1^2/S_2 \qquad (12)$$

where $S_1 = \sum_{m=2}^{M} A_m \hat{Y}_m \exp\left(\frac{-m^2}{4}\tau T_n\right)$

$S_2 = \sum_{m=2}^{M} A_m^2 \exp\left(\frac{-m^2}{4}\tau T_n\right)$

$S_2 = \sum_{m=2}^{M} A_m^2 \exp\left(\frac{-m^2}{4}\tau T_n\right)$

$\tau = 7.27 \times 10^{-12}/M\Delta\sigma^2\lambda_0^2$

re

T_n = neutral gas temperature

$$A_0 = 1/2\pi$$

$$A_m = \frac{R^n}{\pi} \exp\left(\frac{-n^2\pi^2}{4(\ln 2)N_2^2}\right) \operatorname{sinc}\left(\frac{n\pi}{(\ln 2)^{1/2}N_3}\right) \operatorname{sinc}\left(\frac{n\pi}{(\ln 2)^{1/2}N_4}\right)$$

I_0 = intensity = S_1/S_2

C = background continuum = $\frac{\hat{Y}_{\ell 2}}{2} - A_0 I_0$

Only the neutral temperature is unknown. It is determined by iteration (+/- 1°K) of equation 12 in which the least squares difference uniquely determines the temperature.

The uncertainty associated with the retrieved temperature is calculated by representing equation 11 as a function of intensity, neutral temperature, and the Fourier coefficients.

$$\langle \delta y^2 \rangle = \sum_{m=2}^{M} \left[I_0 A_m \exp\left(\frac{-m^2}{4} \gamma T_n\right) - \hat{Y}_m \right]^2 \qquad (13)$$

These variables are linearly expanded about a mean value. The least square error is found by minimizing the equation with respect to the first order approximation for both temperature and intensity error (ie. ΔT and ΔI, respectively). Solution of the resulting matrix yields the least square temperature and intensity errors, known as the variances.

If it is assumed that the random noise superimposed on the signal is Gaussian, the bias is computed by the same procedure with a standard deviation equal to the square root of the signal intensity included. The mean square error is

then calculated as the square root of the sum of the variance and the bias squared.

$$\text{mean square temperature error} = \overline{\Delta T} = \left[\frac{\alpha}{N I_o}\left(1 + \frac{\beta C}{\alpha I_o}\right)\right]^{1/2} \qquad (14)$$

where $$\alpha = \frac{1}{\pi^2}\int_0^{\Delta\chi} \frac{\gamma_i(\chi_i)}{I_o}\,\psi(\chi_i)\,d\chi$$

$$\beta = \frac{1}{\pi^2}\int_0^{\Delta\chi} \psi(\chi_i)\,d\chi$$

$$\psi(\chi_i) = \frac{16\Delta\chi}{\gamma^2}\sum_{m=2}^{M}\cos^2(m\chi_i)\,\frac{\dfrac{A_m \exp\left(\frac{-m^2}{4}\gamma T_n\right)}{\{A_m^2\}} - \dfrac{m^2 A_m \exp\left(\frac{-m^2}{4}\gamma T_n\right)}{\{m^2 A_m^2\}}}{\dfrac{\{m^4 A_m^2\}}{\{m^2 A_m^2\}} - \dfrac{\{m^2 A_m^2\}}{\{A_m^2\}}}$$

bracketed quantities are: $$\{Q_m\} \equiv \sum_{m=2}^{M} Q_m \exp\left(\frac{-m^2}{2}\gamma T_n\right)$$

Derivation of the above equations requires lengthy manipulation and is not included here. However, the expression for the mean square error has been reworked according to the derivation by Hays and Roble and is included as part of the reduction program.

Discussion

The temperature reduction routine utilized the data from the FPI profiles (etalon temperature, etalon pressure, signal intensity, and meridional angle of observation) and from the MSP (6300A intensity at the FPI angle of observation). The information, stored on the MSP data tapes, is transferred to an FPI data tape which is compatible with the University of Alaska, Honeywell computer system. Reduction

of an entire night's data is accomplished directly from the FPI data tape.

In order to check the computer hardware and the analysis program, real-time output from the terminal and X-Y chart recorder was compared with the digital output and plots from the computer data files. Synthetic profiles of known temperatures were constructed for execution by the analysis program. The output temperature agreed well with the synthetic profiles.

As the signal-to-noise ratio improves, the error bar associated with a given profile decreases. In general, a small signal intensity corresponds to a large error bar as shown in Figure 7. If the auroral signal is varying rapidly, normalization of the FPI signal ($.4^{o}$ field of view) with the MSP 6300A intensity (1.5^{o} field of view) is not exact. In addition, the magnitude of the error bars may vary for the same apparent auroral intensity as intensity is averaged over several minutes.

Figure 7 also shows the importance of the 6300A filter. The magnitude of the calculated uncertainty in the narrow filter is less than for the wide filter although calculated errors are greater than predicted assuming purely Gaussian noise.

The retrieved intensity of the fringe profile is proportional to the area under the fringe above a constant background. Figure 8 shows a plot of the intensity of the

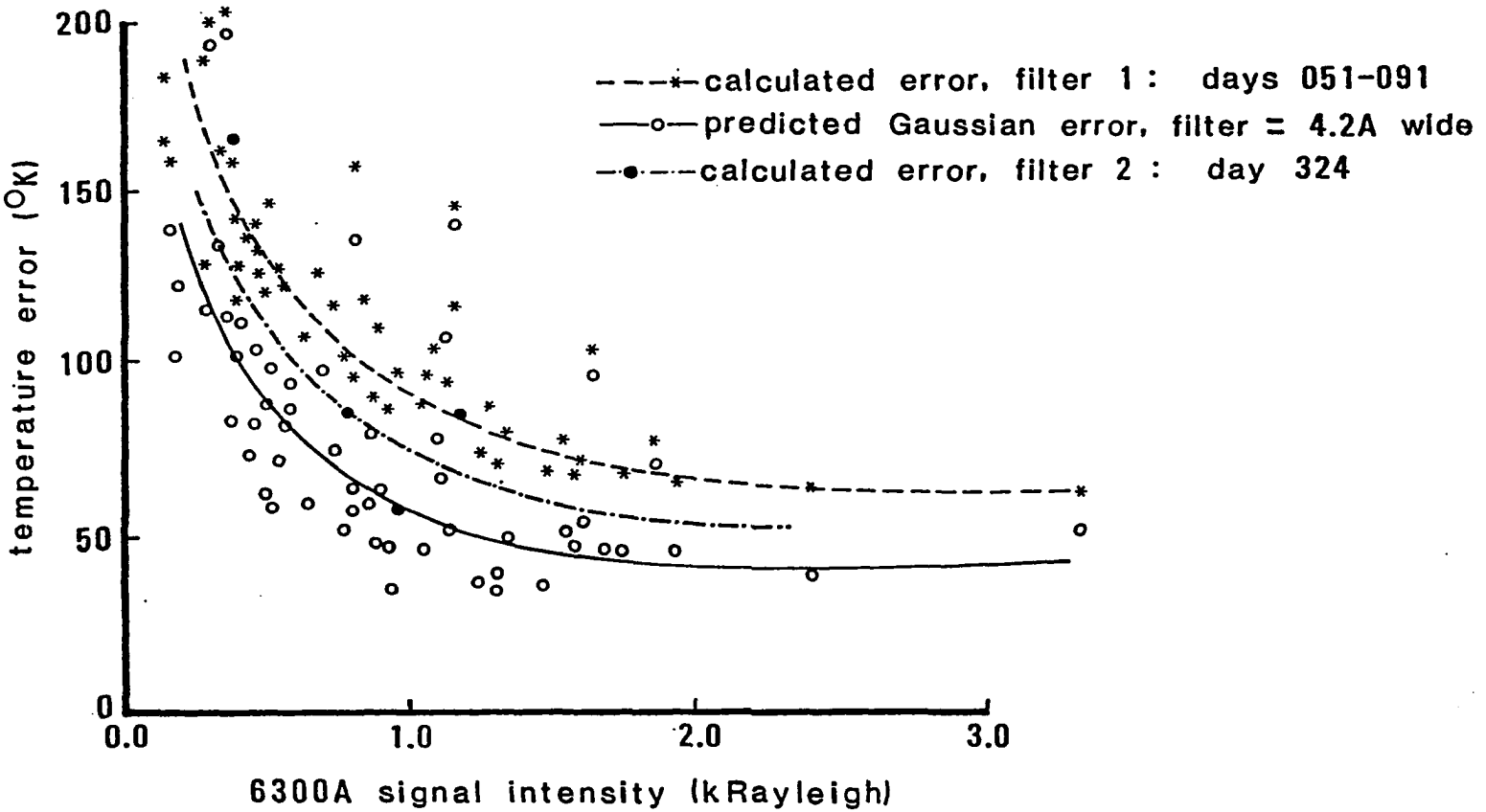

Figure 7. Retrieved temperature error vs signal intensity.

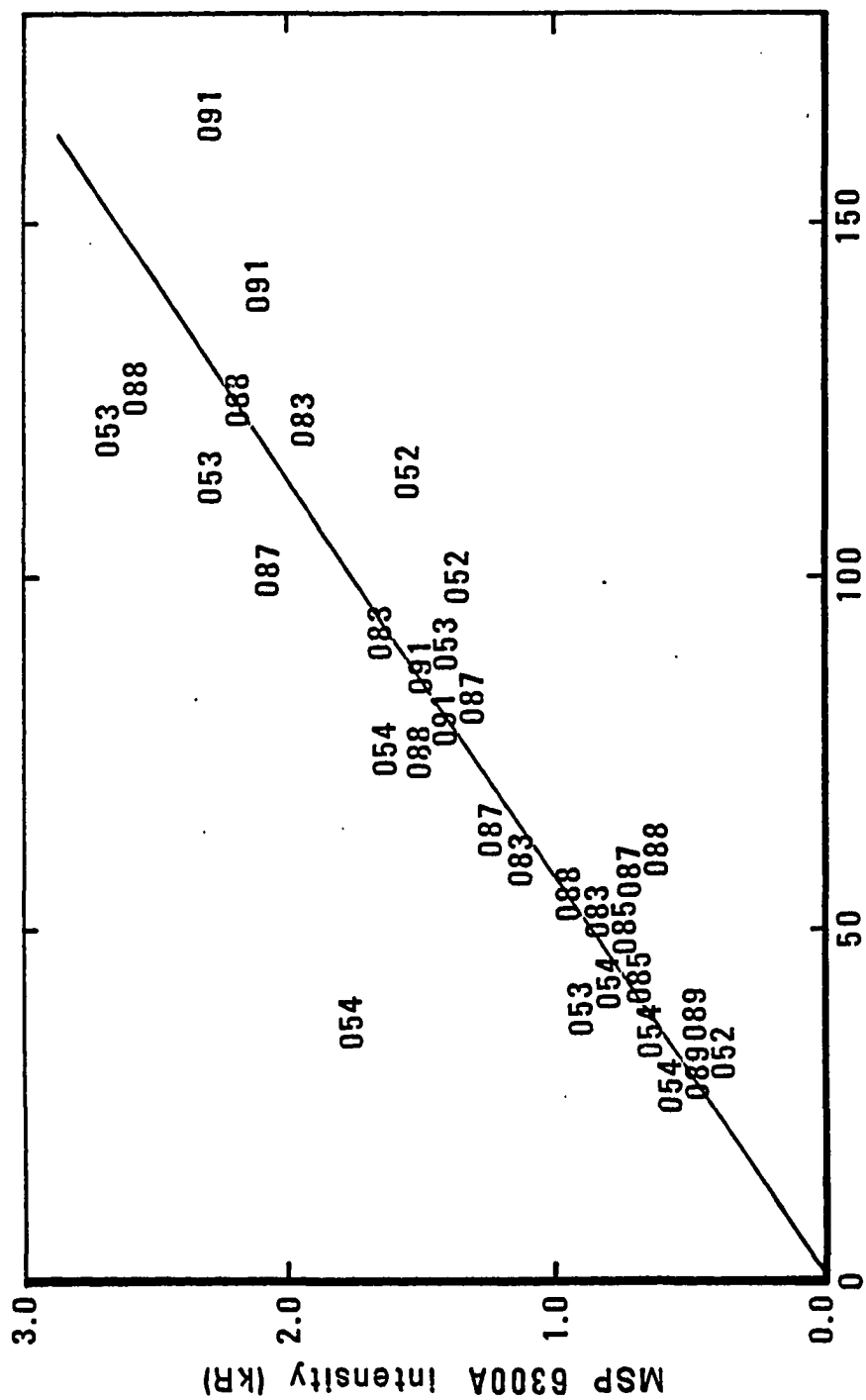

Figure 8. FPI vs MSP 6300A signal intensities, as indicated by the UT days.

6300A emission, calculated from the FPI for the same observation angle for several UT days. The MSP has a broader filter preceding its photometers, a shorter time base of observation, and a different size of field of view so a perfect comparison is not expected.

VI. ANALYSIS

Altitude

Information about the neutral thermosphere is inferred from the line shape of the 6300A $O(^1D) \rightarrow O(^3P_2)$ emission in the auroral spectrum. However, the spatial distribution of the 6300A emission can cause serious difficulties when analyzing temperature data. The problems are caused primarily by the variation in the altitude of the emission profile and its large vertical extent.

Due to the vertical temperature gradient in the atmosphere, meaningful interpretation of the temperature retrieved from the profiles of the 6300A line requires knowledge of the altitude distribution of the emission. In fact, it is often not possible to analyze neutral temperature from data retrieved with a Fabry-Perot interferometer because of the changes in altitude (Hays et al., 1979).

If photometric monitoring equipment is available at geographically separated locations, some information about the height of the maximum emission of 6300A can be obtained by triangulation. In practice, the large vertical and horizontal extent of the emission coupled with both the spatial and temporal variations in the height profiles, makes this a difficult technique to use and often fraught with error. Alternatively, the mean altitude of emission may be

modeled from other experimentally determined quantities.

The altitude for the production of $O(^1D)$ depends strongly on the characteristic energy of the incident particle flux. Since quenching of $O(^1D)$ is primarily altitude dependent, the observed intensity of 6300A varies greatly. In contrast, due to the short radiative lifetime (10^{-8}sec) of the $N_2^+B^2\Sigma_g^+$ state, the intensity of the 4278A emission band is directly dependent on the particle energy input which ionizes N_2.

Rees and Luckey (1974) have used the 4278A intensity and the 6300A/4278A intensity ratio to infer a characteristic energy of the incident auroral particle flux. Using a modified version of the method, with updated rate coefficients and cross sections, a time independent model was developed to calculate the intensity profiles for the 6300A and 4278A emissions for varying characteristic energies. Computation of the profiles begins by assuming a model atmosphere with a 750^oK exosphere and with known densities of N_2, O_2, O, and electrons. Production profiles of O_2^+ and $N(^2D)$ are calculated so that the production profile for $O(^1D)$ can be determined based on the following production reactions.

$$O(^3P) + e^-(E > 1.96eV) \longrightarrow O(^1D) + e^- \quad (15)$$

$$O_2^+ + e^- \longrightarrow O(^1D) + O(^3P, {}^1D, {}^1S) \quad (16)$$

$$N(^2D) + O_2 \longrightarrow O(^1D) + NO \quad (17)$$

(Hays et al., 1978 and Rusch et al., 1978).

During periods of low energy flux, reaction (15)

produces a maximum in $O(^1D)$ production near 260km. With higher energy flux, deeper penetration of electrons may allow maximum production to occur as low as 120km (Vallance-Jones, 1974). Both dissociative recombination and atom-atom interchange (reactions 16 and 17) require the presence of the heavier molecular ions so that maximum production generally occurs below 150km.

De-excitation of $O(^1D)$ is due primarily to collisions with molecular nitrogen and oxygen and to spontaneous emission.

$$O(^1D) + N_2 \longrightarrow O(^3P) + N_2 \qquad (18)$$

$$O(^1D) + O_2 \longrightarrow O(^3P) + O_2 \qquad (19)$$

$$O(^1D) \longrightarrow O(^3P) + h\nu(6300A) \qquad (20)$$

Due to the high concentration of O_2 and N_2 at lower altitudes and to the long radiative lifetime of $O(^1D)$, quenching below 200km is extremely rapid. The quenching rate coefficients for reactions 18 and 19 are of the same order of magnitude, but the greater abundance of N_2 causes it to be the dominant quenching species (Rusch et al., 1978).

The combined production and quenching of $O(^1D)$ produce the emission profiles for 6300A. The altitude of emission is generally between 190 and 250km. Figure 9 shows the emission profiles for several characteristic energies of the particle flux incident on the atmosphere. The figure may be used to determine the mean altitude of the emission.

A 6300A/4278A intensity ratio is determined by the

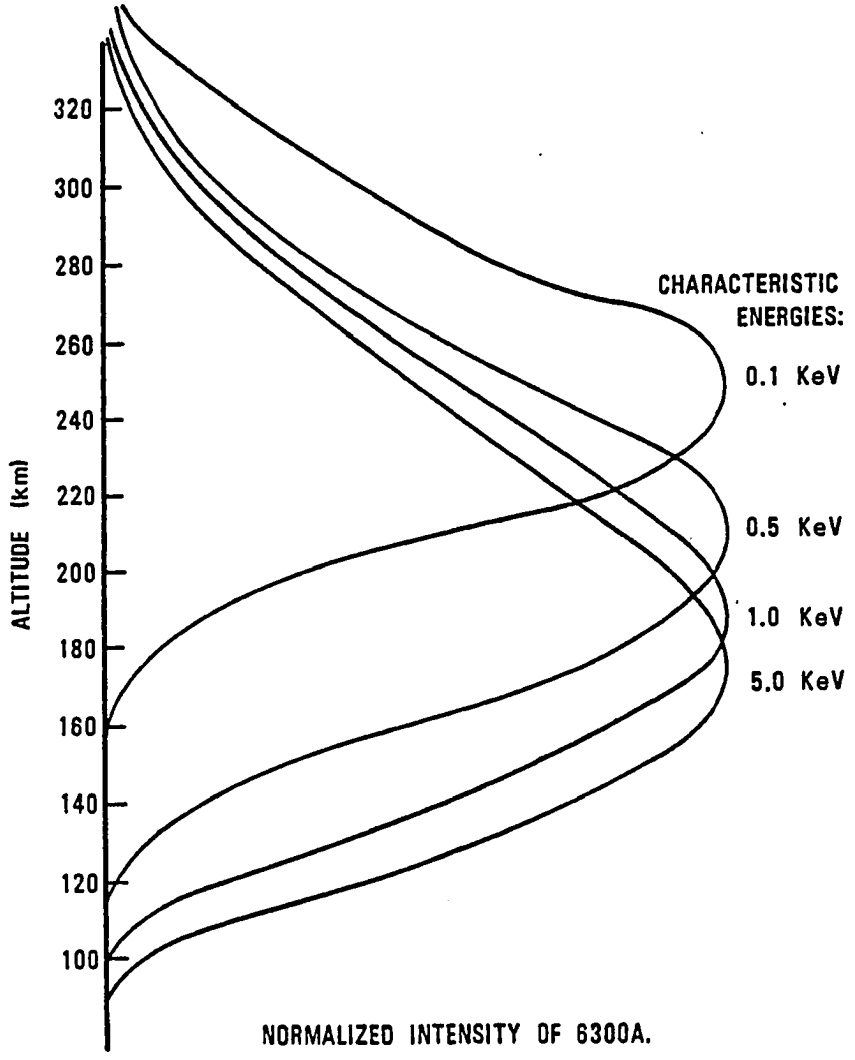

Figure 9. Emission profiles of 6300A for varying characteristic energies.

model from the height-integrated, volume emission profiles of the 6300A and 4278A emissions, respectively. The intensity of 6300A is determined from the emission profiles in Figure 9. The intensity of the 4278A emission is calculated from equation 25 (discussed later) for assumed ionization rates.

In summary, the input characteristic energy in the model uniquely defines the 6300A intensity profile (and hence the mean altitude of the 6300A emission) as well as the ratio of the 6300A and 4278A intensities. A plot of the mean altitude of 6300A emission for a given ratio is shown in Figure 10. (The characteristic energy has been assumed nearly constant for varying 4278A intensities.) In practice, the 6300A/4278A ratio is determined from the Meridian Scanning Photometer data. Use of the ratio method determines characteristic energy and the mean altitude of the 6300A emission. This method for determining altitude is valid only if the two emissions originate from the same incident energy distribution. Thus the ratio (and hence the altitude) can be inferred only for data along the geomagnetic field lines (103^{o} elevation).

Another problem encountered during temperature analysis is revealed by the emission profiles in Figure 9. The large vertical extent of the emission coupled with a significant temperature gradient implies that the total observed emission may well originate from regions that vary by several

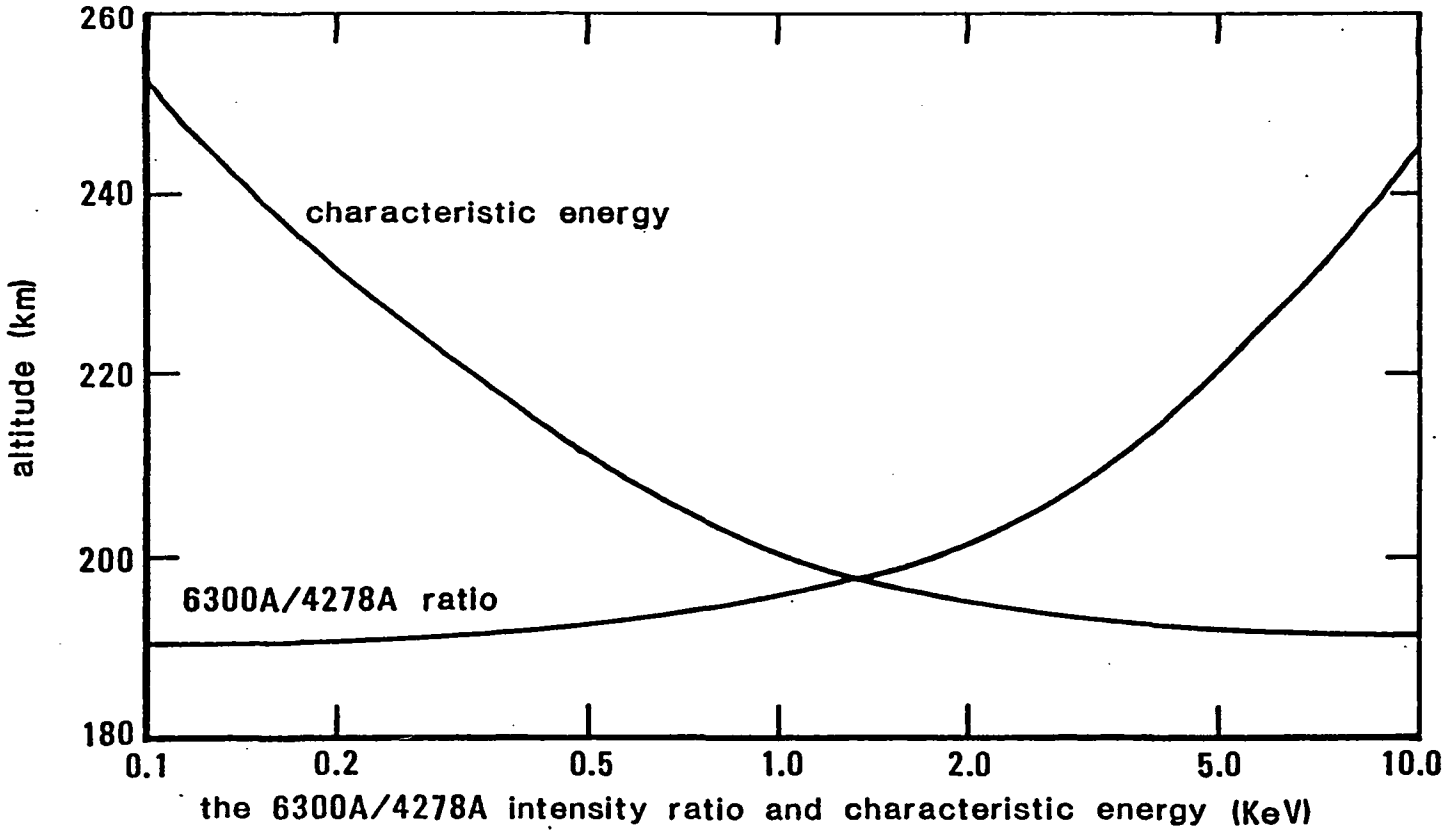

Figure 10. Mean altitude of 6300A emission vs characteristic electron energy and 6300A/4278A intensity ratio.

hundred degrees Kelvin. Thus, the received 6300A signal is a composite signal originating over a range of height and temperature regimes.

Using the same model as previously, the integrated effect due to observing a column emission is simulated by constructing synthetic signals. The signal is a composite of Doppler broadened spectral lines determined from the kinetic temperatures at several altitudes in the emission profile and weighted by the intensity of the emission at each altitude. The composite signal is analogous to the signal received by the FPI and defines a single temperature which can then be compared with the temperature at the mean altitude. Figure 11 shows the results of the comparison and is used to determine the neutral temperature (T_N) at the mean altitude, given the retrieved FPI temperature (T_{FPI}) and the 6300A/4278A intensity ratio.

The above discussion emphasizes some of the difficulties encountered when using the line width of the 6300A emission to derive the neutral temperature. The above method for determining the neutral temperature at the mean altitude is used in the presentation and analysis of all FPI data presented in this thesis. Their use is justified since the average lapse rate, determined by the application of these techniques to the temperatures from the FPI, agrees well with the lapse rate predicted by the several atmospheric models for the time and location of observation

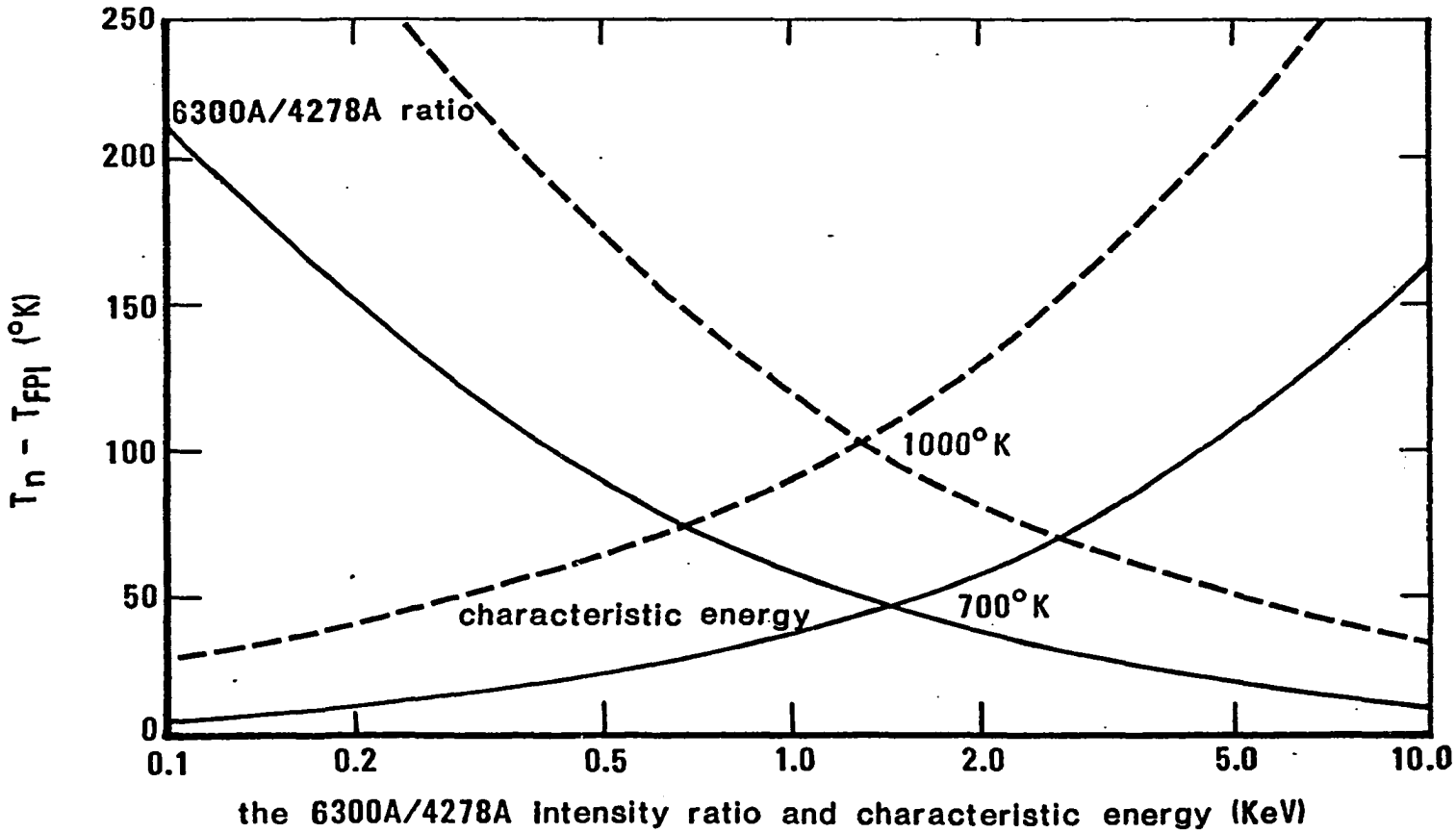

Figure 11. Correction for column emission effects vs characteristic electron energy and 6300A/4278A intensity ratio for 700° and 1000°K exospheres.

(Figure 13, discussed later).

Heating

The atmosphere is heated by the aurora primarily through auroral electric fields and particle bombardment.

The first source of auroral heating is dependent on the behavior of charged and neutral particles in electric and magnetic fields. Assuming, for the moment, that there exists no electric field and no collisions, ions and electrons will gyrate in the earth's magnetic field ($\vec{B}$) in opposite directions. The radii of the gyrations (or Larmor radii) are proportional to their respective masses while the gyrofrequencies are inversely related to the mass.

Frequently, prior to the onset of an aurora, a large electric field will occur causing strong currents known as the auroral electrojet. The electric field ($\vec{E}_\perp$) is primarily perpendicular to $\vec{B}$ and, in the "collisionless" plasma, the subsequent ion and electron motions are described by the force equation.

$$\text{Force equation} = m\vec{a} = q(\vec{E}_\perp + \vec{v} \times \vec{B}) \qquad (21)$$

where m = mass

$\vec{a}$ = acceleration

v = velocity

q = charge

The motions remain generally circular with an added transverse component known as the plasma drift. The drift for both ions and electrons is in the $\vec{E}_\perp x \vec{B}$ direction.

In the atmosphere, neutral particles, unaffected by $\vec{E}_\perp x\vec{B}$, interrupt the flow of the charged species through collisions. If $\nu_i, \nu_e << \omega_i, \omega_e$ (where ν_i, ν_e are the ion and electron collision frequencies and ω_i, ω_e are the ion and electron gyrofrequencies), then equation 21 describes the ion and electron motions.

However, with decreasing altitude the number of collisions per gyration increases. Due to the larger Larmor radius and the smaller gyrofrequency of the ions, ion drift will begin to shift in the direction of $\vec{E}_\perp$ while electron drift is only slightly changed. The resulting current is described by the generalized Ohm's law.

$$\text{Generalized Ohm's law} = \vec{j} = \vec{\vec{\sigma}} \cdot \vec{E} \qquad (22)$$

where $\vec{j}$ = current

$\vec{\vec{\sigma}}$ = conductivity tensor

In the atmosphere, auroral heating from the presence of electric fields (ie Ohmic heating) is primarily due to the flow of current in the direction of the electric field (or Pedersen current). The amount of heating is described using the Pedersen conductivity and the magnitude of the electric field.

$$\text{Ohmic heating} = H_o = \int_h \sigma_p E_\perp^2 dh \qquad (23)$$

where h = height

σ_p = Pedersen conductivity (modeled from radar data)

The Pedersen conductivity, and hence Ohmic heating, is generally maximum where $\omega_i < \nu_i$ and $\nu_e < \omega_e$.

As the collision frequencies continue to increase so that $\omega_i, \omega_e < \nu_i, \nu_e$, differential flow between ions and electrons is primarily in the $\vec{E}_\perp \times \vec{B}$ direction producing the Hall current. Since the Hall current is perpendicular to the electric field, it does not produce Ohmic heating. However, some Ohmic heating occurs when the ion and electron flow is restricted through the collisions with the neutral particles.

Due to their similar masses, heating of the neutral atmosphere occurs primarily through collisions with ions, contributing approximately half of the energy input to the neutral gas. However, the greater thermal mass of the neutral atmosphere causes it to be more sluggish than the ion atmosphere in its dynamic response to energy input. Since the neutral gas acts as a heat sink for the ions, the ion temperature may be greater than that of the neutrals.

The second source of auroral heating is through auroral particle bombardment by energetic electrons and protons. These give rise to secondary electrons through ionizing collisions with neutrals. Neutrals are then heated through ionic recombination, chemical reactions, and ion-neutral and electron-neutral collisions.

$$\text{Particle heating rate} = H_p = \int_h E(h)\, Q_{ION}(h)\, dh \qquad (24)$$

where $E(h)$ = heating efficiency

Q_{ION} = ionization rate/unit volume

An average of one ion-electron pair is produced for roughly every 35eV lost by the primary electron (Chamberlain, 1961). Thus, particle energy input can be approximated if the ionization rate is determined.

Two sources of data (radar and optical) afford two methods for deriving the ionization rate. Since the 4278A transition is fully allowed and is directly proportional to the excitation rate of $N_2^+ B^2\Sigma_g^+$ (discussed previously), an optical method for determining ionization rate is through measurement of the 4278A intensity. Production of the $N_2^+(0,1)$ band, and hence the 4278A radiation, is approximately 1/52 the ionization rate of N_2^+ (Vallance-Jones, 1974).

$$Q_{ION} \simeq \frac{52 \times I(4278)}{.76 \times F_{N_2}} \qquad (25)$$

where F_{N_2} = relative frequency of ionization of $N_2 \simeq \frac{.94[N_2]}{.94[N_2]+.55[O]+[O_2]}$ (numerical parameters represent relative magnitude of the peak value of the laboratory-determined cross section)

$[N_2],[O_2],[O] \simeq$ neutral densities

$I(4278)$ = volume emission rate of 4278A (MSP data)

The second method for determining ionization rate utilizes electron density profiles determined by incoherent

scatter radar data. In a steady state, the rate of ionization equals the rate of ionic recombination. In the 120km region, the density of negative ions is negligible and the rate of recombination is proportional to the product of the ion and electron densities. Assuming charge neutrality, ion and electron densities are equal and the rate of ionization of the neutral atmosphere through auroral particle bombardment is calculated.

$$Q_{ion} = \int_h k N_e^2 \, dh \qquad (26)$$

where $k(h)$ = effective recombination coefficient

$N_e(h)$ = electron density (radar data)

The effective recombination coefficient may be calculated by measuring the time rate of change of electron density during periods of little or no ionization. Equation 26 is a valid approach for determining ionization in the E region, but in the F region it is strictly an approximation.

Convection and Composition

In the following analysis, neutral temperature (FPI data) will be compared with ion and electron temperatures (radar data). The ion and electron temperatures deduced from the radar data are dependent on the average mass of the ion atmosphere.

During quiet conditions, the pressure diffusion law predicts diffusive separation of atmospheric constituents by molecular weight above approximately 120km. Because atomic

oxygen has a lighter mass than neutral molecules, it is generally the dominant neutral species near 200km and above. Ionized atomic oxygen is the dominant ion species.

During auroral activity, mixing of the constituents occurs as auroral heating of the atmosphere may give rise to vertical convection (Hays et al., 1973). Neutral molecules are transported upwards from lower altitude regions and, through ionization, molecular ions are formed.

For radar determination of ion and electron temperatures, the ion composition at 200km and above is generally assumed to be 100% O^+. However, if mixing and convection occur, the ion composition may be altered and remain changed for several hours following auroral heating. The molecular weights of NO^+ and other molecular ions are indistinguishable from one another, but their combined presence with the smaller mass of O^+ will substantially alter the calculated values for ion and electron temperatures.

Calculations reveal that if the mean ion mass is higher than assumed (i. e. if less than 100% O^+ exists), then the deduced ion and electron temperatures will be erroneously small. Figure 12 and the following equations describe the correction coefficients for different atmospheric ion compositions.

$$T_i(q) = A(q)\,T_i(1) \tag{27}$$

$$T_e(q) = C(q)\,T_e(1) \tag{28}$$

where $$q \equiv \frac{[O^+]}{\sum_x [X^+]}$$

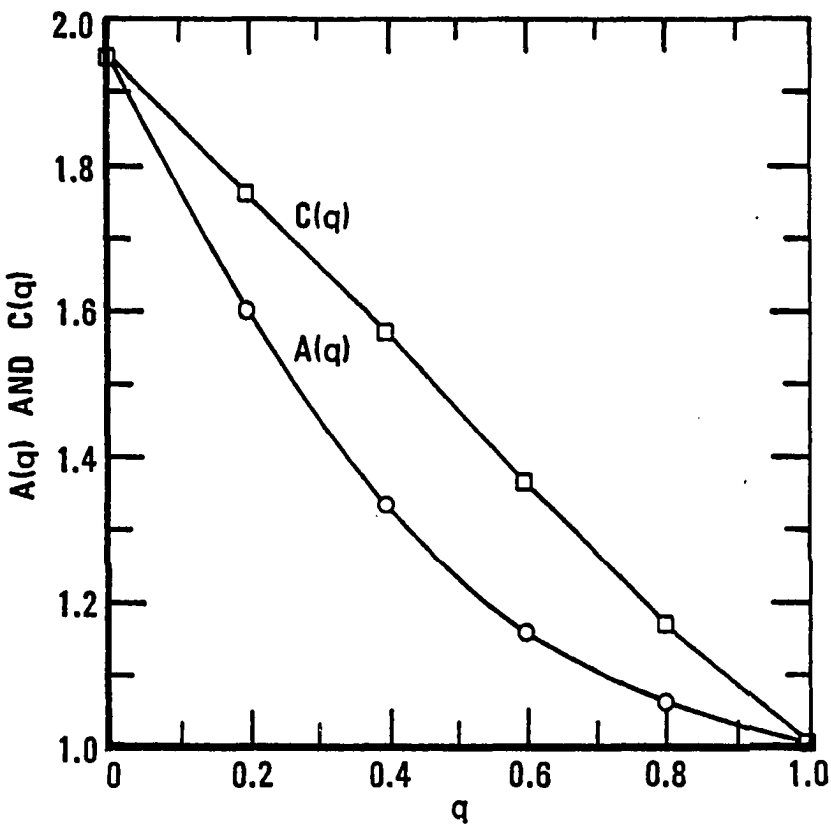

Figure 12. Correction for ion and electron temperatures based on mean ion mass (Source: Kelly, 1979; after Wickwar, 1974).

(Kelly, 1979; after Wickwar, 1974).

The ion and neutral temperatures that are used in this thesis are obtained by independent methods. By imposing the condition that ion temperature be equal to or greater than neutral temperature (discussed previously), information about the ion composition near 200km may be inferred using Figure 12 and equations 27 and 28. The calculations, indicating the approximate percent of O^+ in the atmosphere near 200km, must be interpreted carefully as large errors can exist.

VII. RESULTS

Both the aurora and the calculated neutral temperatures varied greatly during the course of a night's observations. Variations in the mean altitude of emission could substantially affect the neutral temperature deduced by the Fabry-Perot interferometer. The concern was that the observed changes in temperature were primarily due to changes in altitude.

To examine this problem, an experimentally determined lapse rate was calculated for several days from the interferometric and Meridian Scanning Photometer data. Two typical nights are shown in Figure 13. The altitude and neutral temperature were determined as described in Chapter VI.

For day 054 the data points begin with observations near 0700UT and continue through local midnight, 1000UT, until nautical twilight near 1400UT. The regions between the sets of long and short dashed curves bracket profiles predicted by the atmospheric models of Jacchia (1965) and the Mass Spectrometer and Incoherent Scatter (MSIS) of Hedin et al. (1979) between 0700UT and 1300UT. Input for the models are the 10.7cm solar flux, K_p or A_p indices, geomagnetic location, and local time.

The experimental data for the entire day of 054 show a

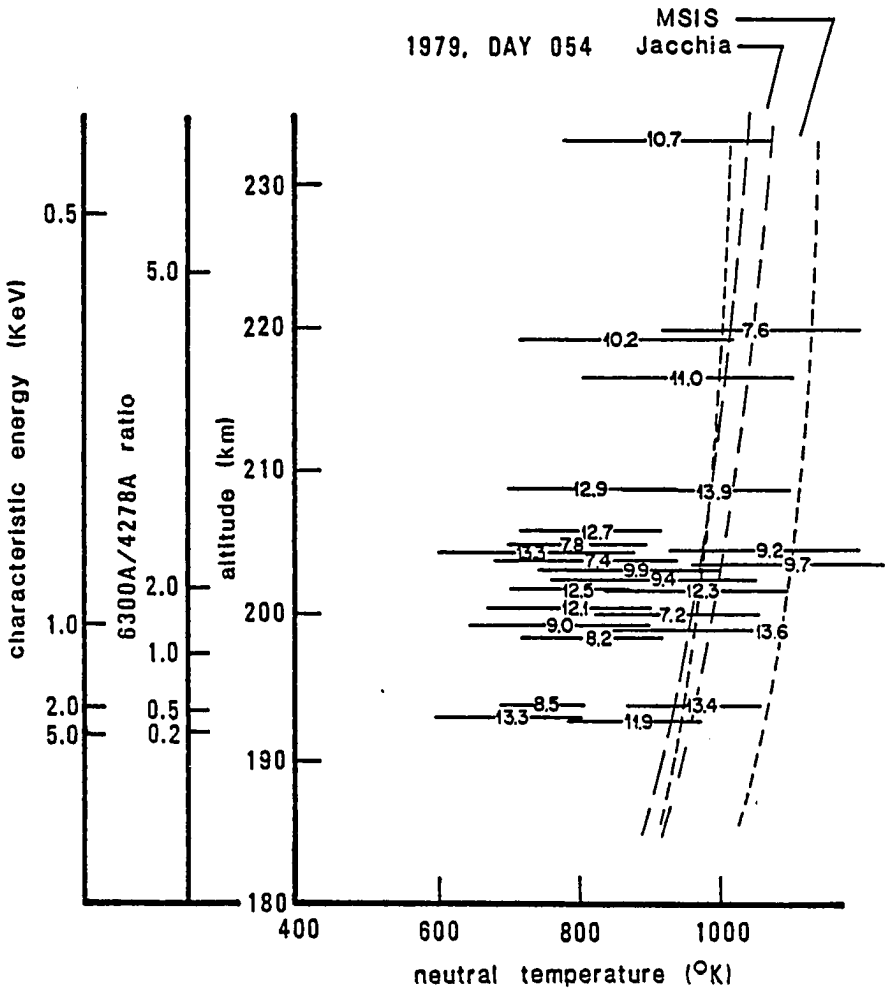

Figure 13a. Retrieved neutral temperatures vs characteristic energy, 6300A/4278A intensity ratio, and mean altitude of emission (predicted using ratio method). The decimal equivalent of the UT time indicates when data were recorded. Jacchia and MSIS model predictions are shown.

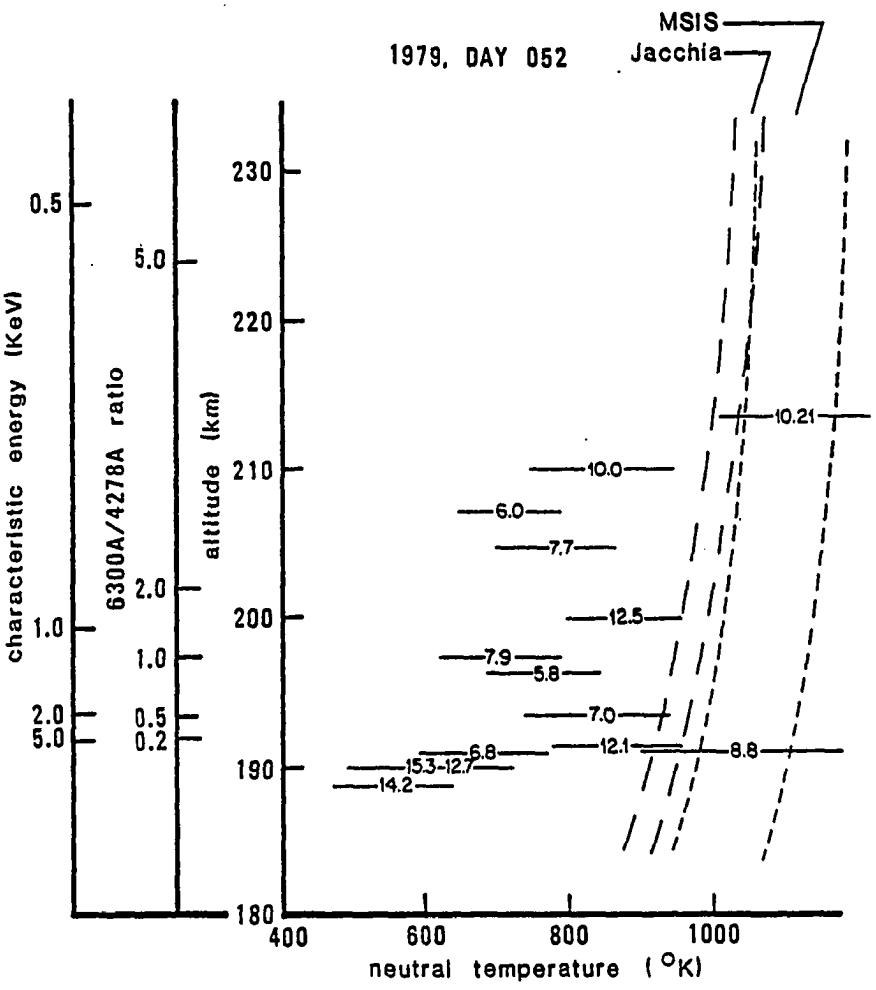

Figure 13b. Retrieved neutral temperatures vs characteristic energy, 6300A/4278A intensity ratio, and mean altitude of emission (predicted using ratio method). The decimal equivalent of the UT time indicates when data were recorded. Jacchia and MSIS model predictions are shown.

lapse rate similar to that predicted by Jacchia and MSIS. The observed lower temperature profile may result from procedural errors or may indicate that the atmosphere is truly cooler than predicted. Deviations from the average curve are toward a warmer atmosphere and may indicate local warming on a short time scale. In any case, the techniques for determining altitude and neutral temperature appear reasonable.

The similarity between the experimental and theoretical lapse rates in Figure 13a suggests that the lapse rate from the Jacchia temperature profiles may be used to adjust the neutral temperature data to a common altitude. Since in the altitude regions where 6300A originates the lapse rate is small, the adjustment in temperature need not be substantial and it effectively eliminates further concern about the altitude of emission. The common altitude of 200km is selected and subsequent neutral temperature data are corrected to this altitude.

For day 052 (Figure 13b) data showing the lapse rate are more scattered. For this day, geomagnetic activity increased substantially from the previous day and variations in the data used to determine the lapse rate suggest that auroral heating may be important in determining the neutral thermospheric temperature.

A sample of the data from the FPI is shown in Figure 14. Approximately half the data were taken at 103^{o}EL and used in the following analysis. Subsequent calculations

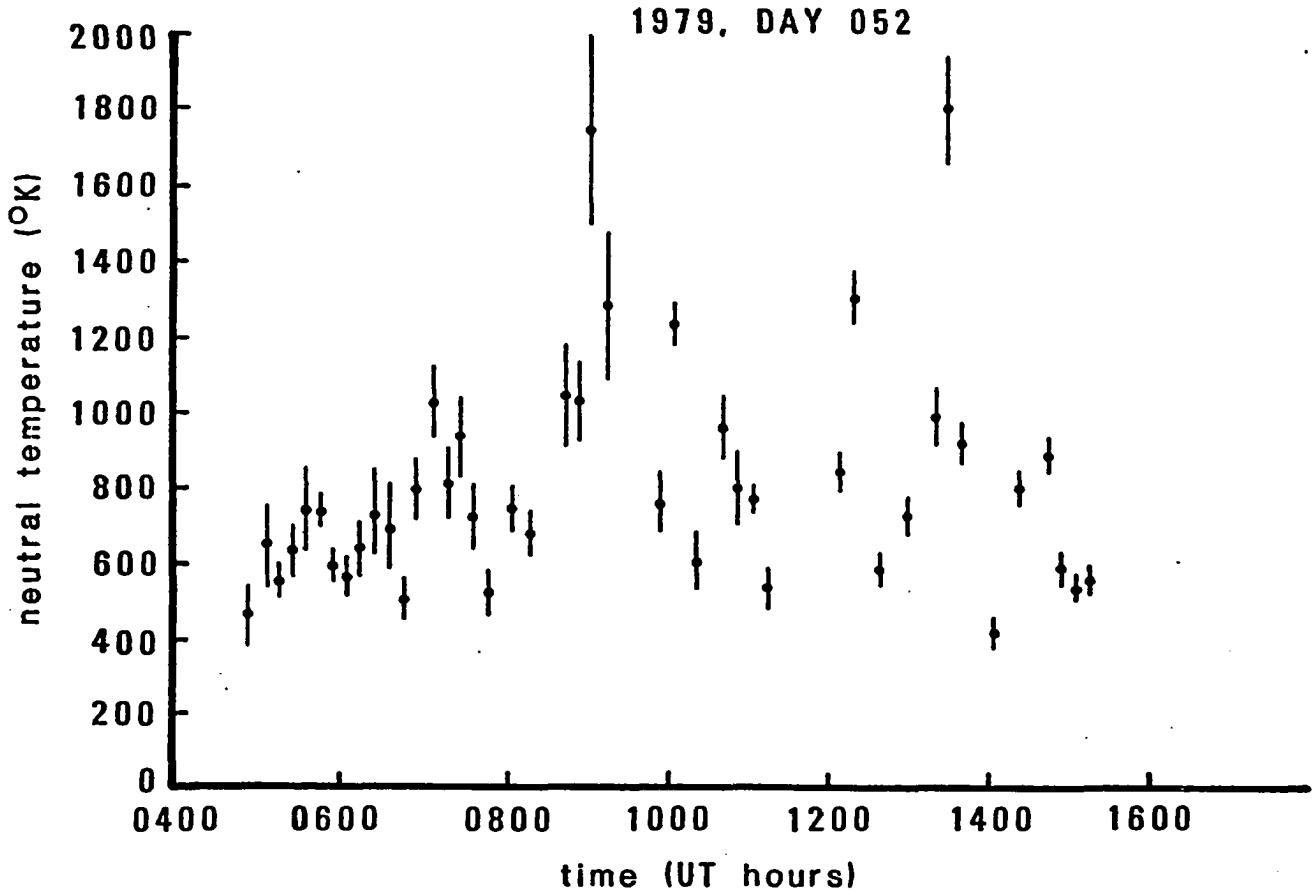

Figure 14. Retrieved neutral temperature for all angles of observation.

from the Meridian Scanning Photometer data were used to infer the mean altitude of emission (Figure 15). Neutral temperature data, adjusted to 200km, are shown sequentially lettered in Figure 16.

For three nights, data were taken during operation of the Thomson Scatter Radar at Chatanika. Ion and electron temperatures were deduced from the radar data assuming a 100% O^+ ion atmosphere (Wickwar and McCready, private communication). These data, interpolated to 200km from data at the 165 and 220km range gates, are also shown in Figure 16. If radar and FPI measurements did not coincide in time, the FPI data were interpolated from the nearest observations at 103^{o}EL.

As discussed previously, due to the similar masses, collisions between ions and neutrals require that ion and neutral heating rates be approximately equal. For the entire night of 052, Figure 17a, the observed neutral and ion temperatures are nearly equal. Their equality, indicating transfer of kinetic energy between neutral and ion species or that no electric fields are present, provides additional justification for the techniques used to deduce neutral temperature from the FPI data.

The electron temperature is expected to be greater than or equal to the neutral temperature. The relationship is shown in Figure 17b.

Simultaneous radar and FPI data exist for days 087 and

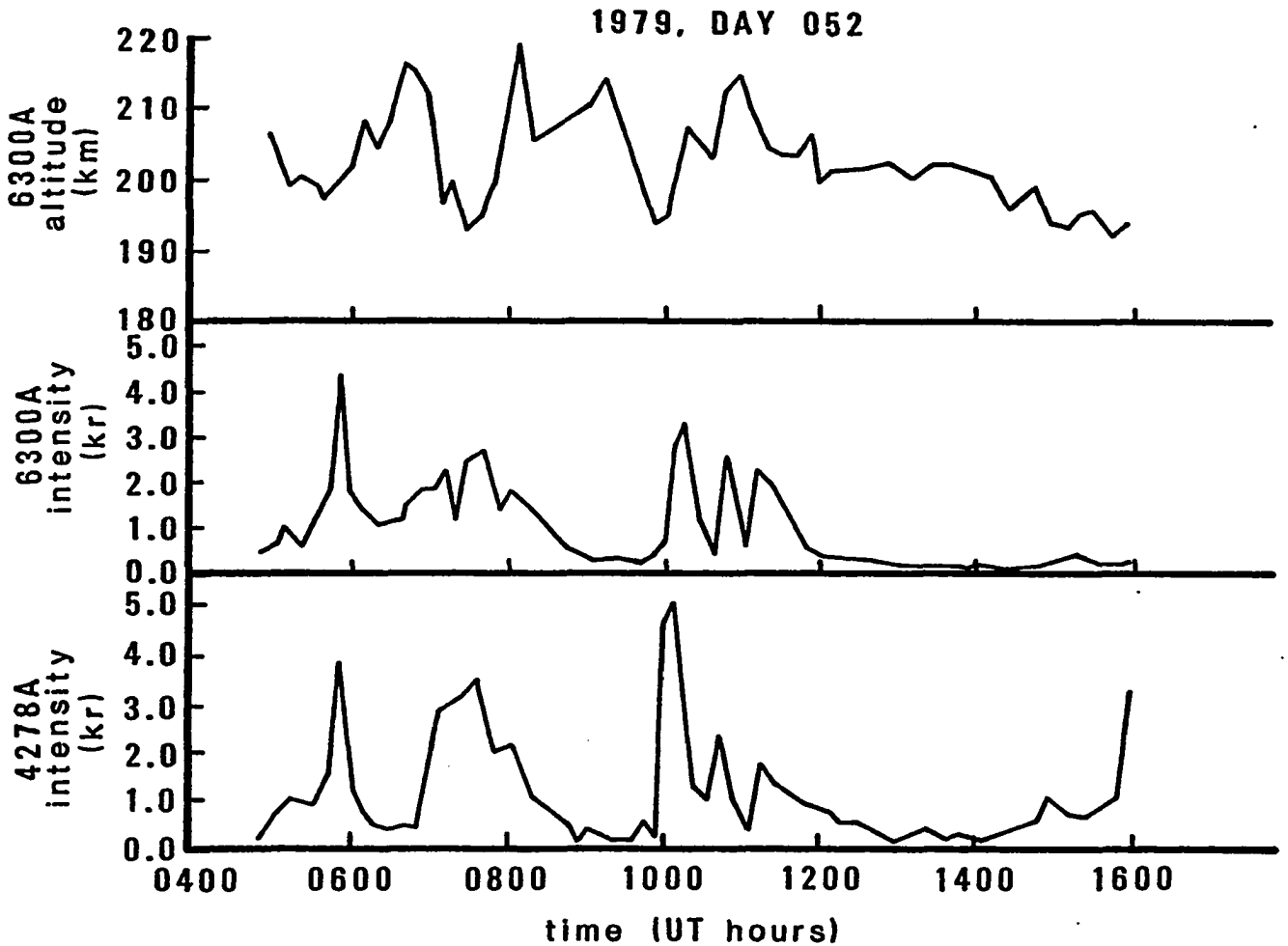

Figure 15. Calculated mean altitude of emission, and 6300A and 4278A intensities.

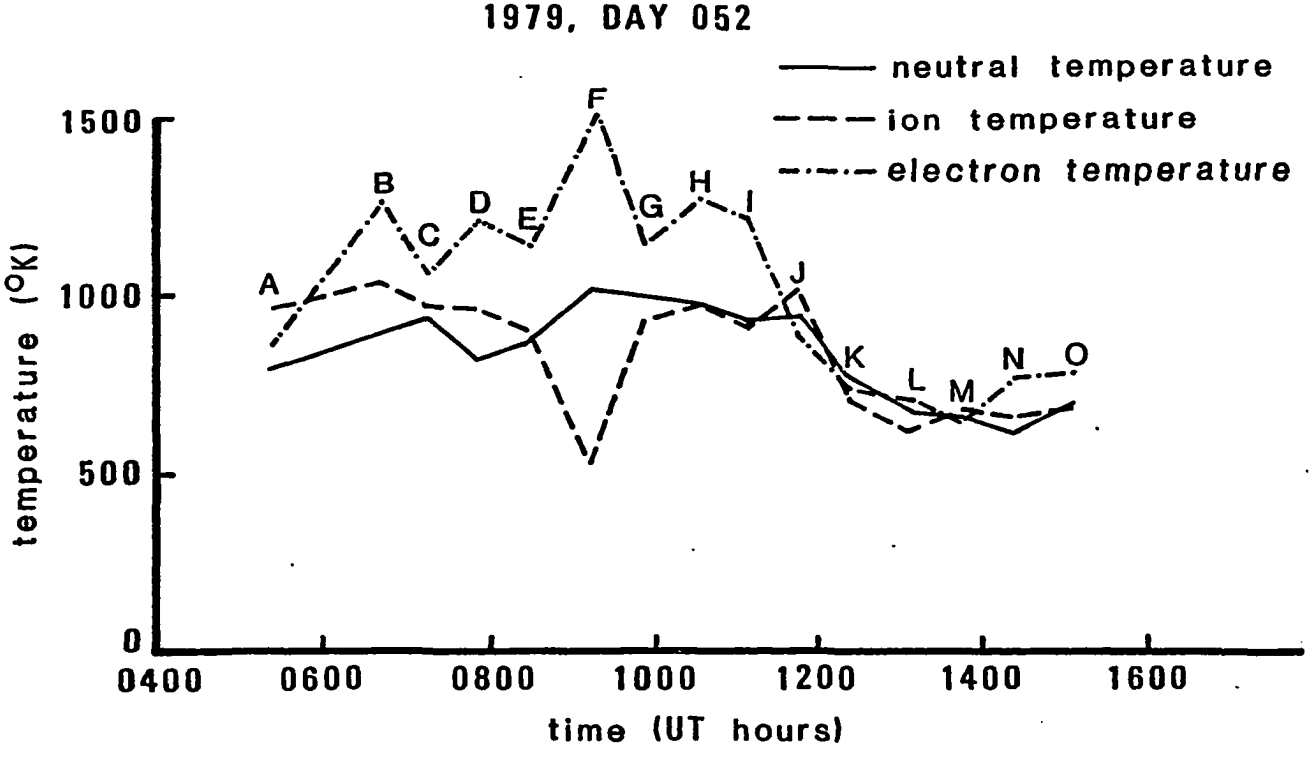

Figure 16a. Neutral, ion, and electron temperatures at 200km for 103°EL. Uncertainties of measurement are shown in Figure 17.

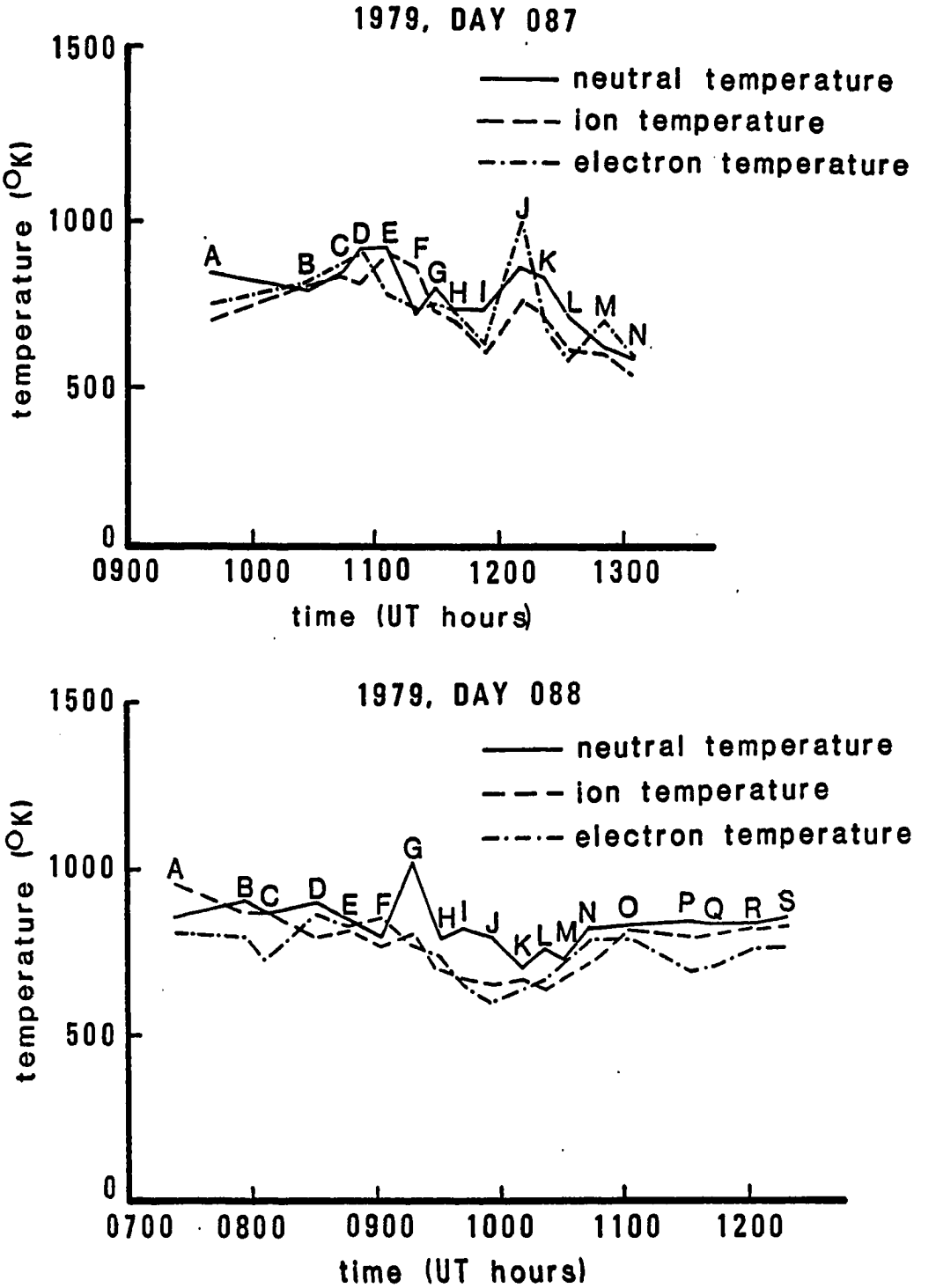

Figure 16b,c. Neutral, ion, and electron temperatures at 200km for 103°EL. Uncertainties of measurement are shown in Figures 18 and 19.

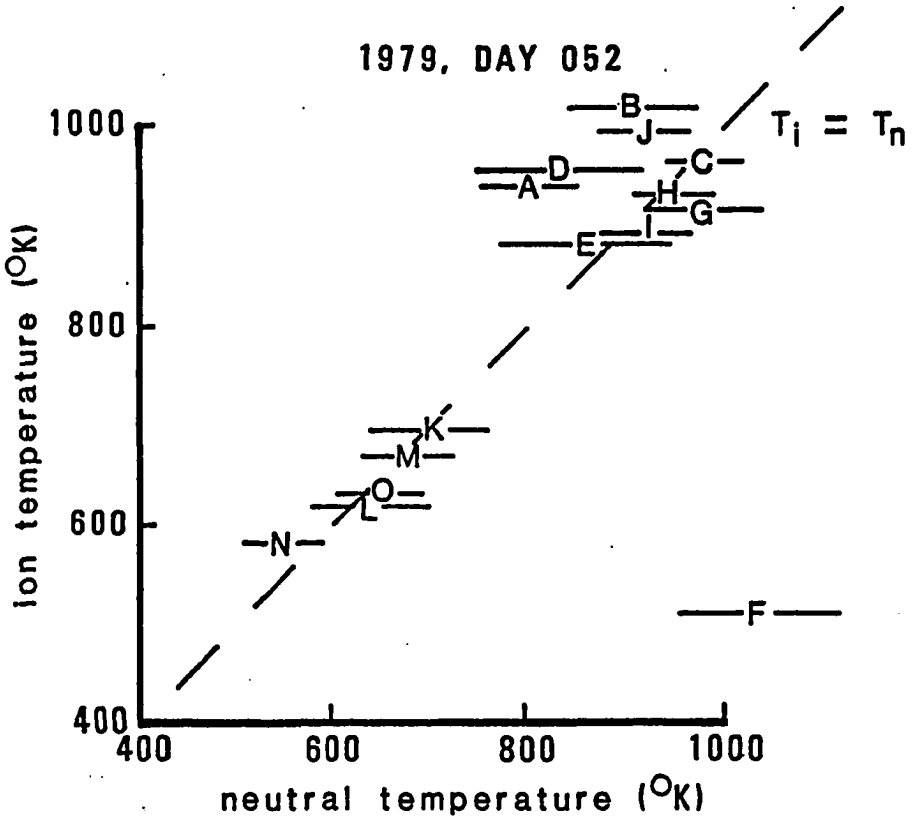

Figure 17a. Neutral vs ion temperature at 200km. Letters correspond to times indicated in Figure 16. A 100% O^+ atmospheric model is used to calculate ion temperature; uncertainty in ion temperature is approximately +/- 90°K.

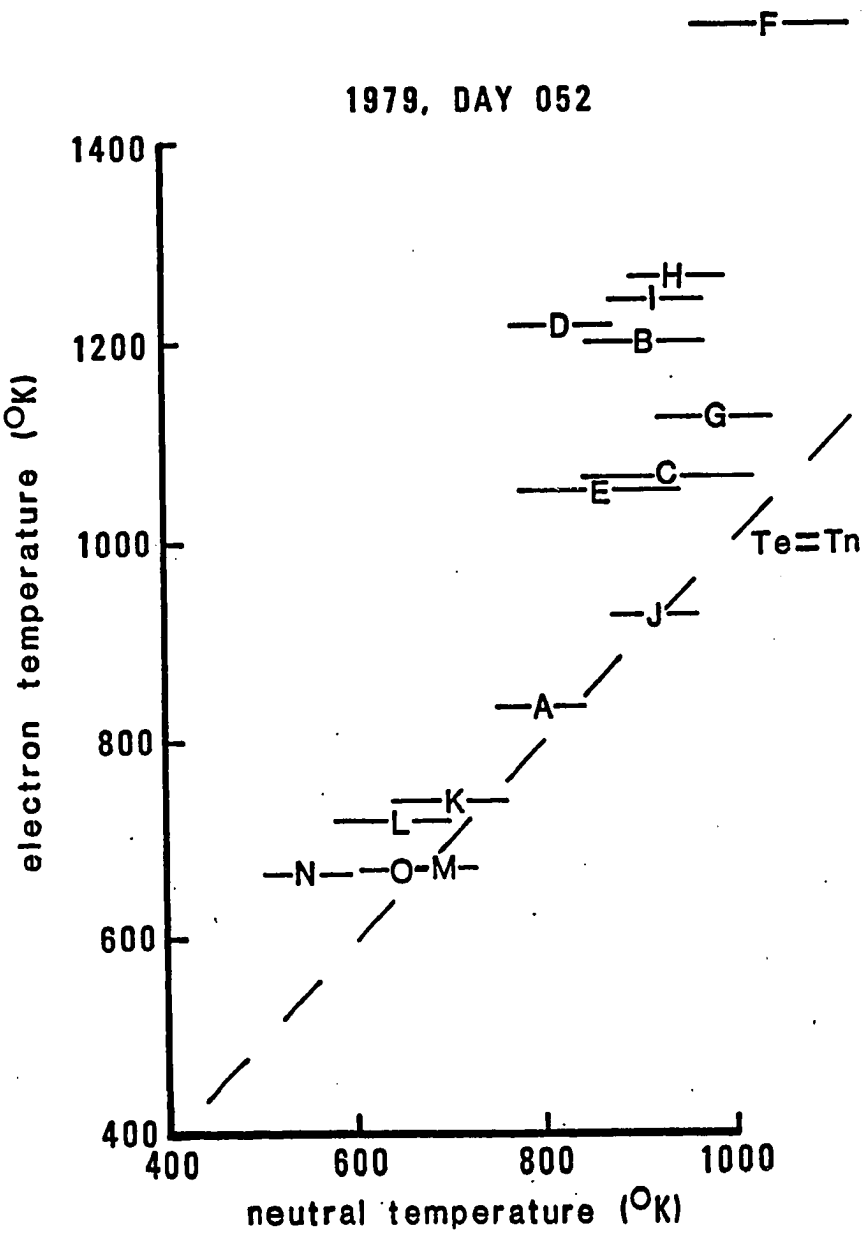

Figure 17b. Neutral vs electron temperature at 200km. Letters correspond to times indicated in Figure 16. A 100% O^+ atmospheric model is used to calculate electron temperature; uncertainty in electron temperature is approximately +/- 90°K.

088 and plots of neutral temperature versus ion and electron temperatures are shown in Figures 18 and 19. For all periods of simultaneous data, neutral temperature is shown generally equal to ion temperature and less than or equal to electron temperature, within the allowed error.

Point F is the most noticeable feature in Figures 16 and 17 and may indicate substantial composition changes in the atmosphere or the conduction or transport of energy from aurorally heated regions. The point corresponds to an unusually high neutral temperature (Figure 14), recorded at 20^{o}EL, as well as the time when a convection cell, rising at radar-determined vertical velocities and originating at 115km near 0740UT, would attain the altitude of 200km.

As discussed in Chapter VI, the percent O^{+} may be calculated by using Figure 12 and equations 27 and 28 and by assuming that ion and neutral temperatures are equal. However, near point F, the predicted percent O^{+} composition varies from 100% to less than 20%. Since a change of this magnitude is unlikely, the data for point F may be erroneous.

For days 087-088 (Figures 18-19), an average of 80% O^{+} may exist near 200km. Data for the total energy input are not available for all periods of observation, but the magnetometer data (Figure 23, discussed later) indicate substantial auroral activity for this period. During this period, the lower boundary for 100% O^{+} may have increased in

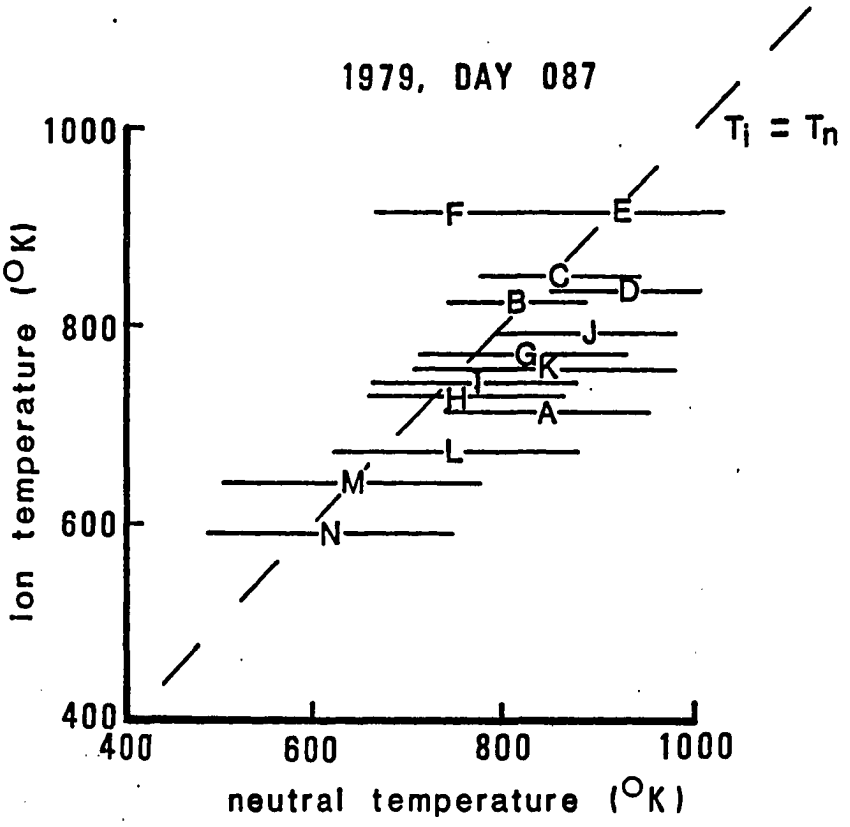

Figure 18a. Neutral vs ion temperature at 200km. Letters correspond to times indicated in Figure 16. A 100% O^+ atmospheric model is used to calculate ion temperature; uncertainty in ion temperature is approximately +/- 70^{O}K to 140^{O}K.

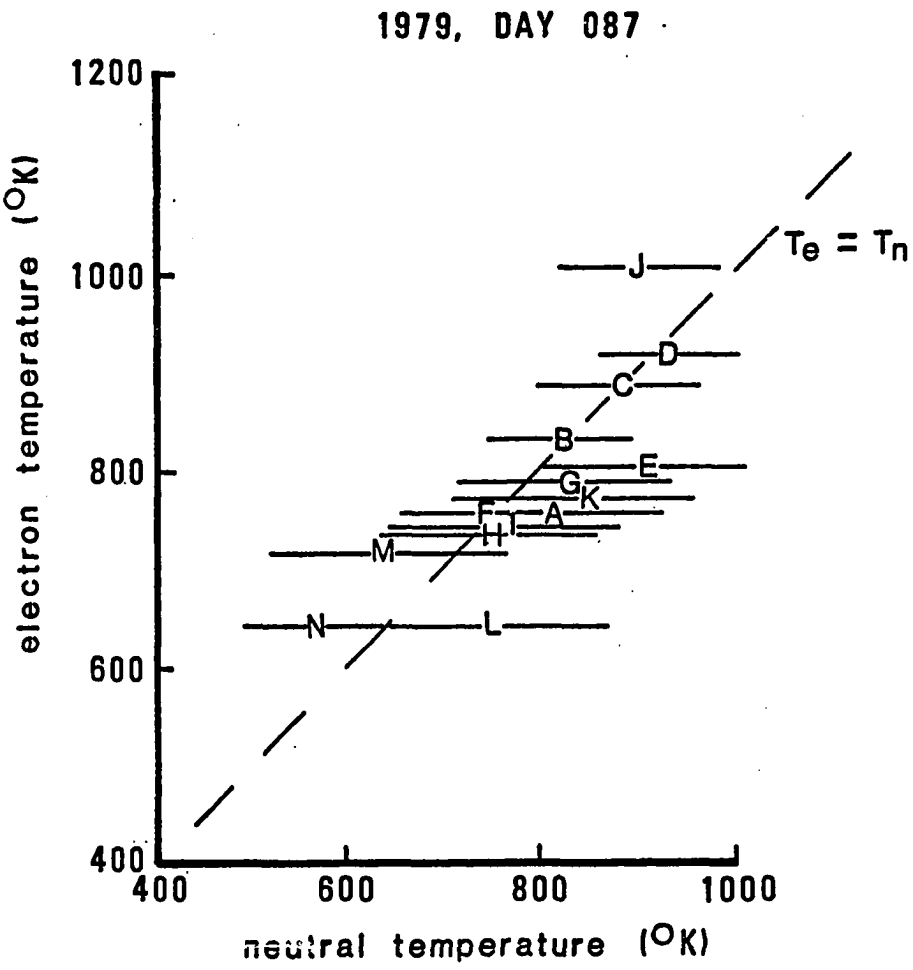

Figure 18b. Neutral vs electron temperature at 200km. Letters correspond to times indicated in Figure 16. A 100% O^+ atmospheric model is used to calculate electron temperature; uncertainty in electron temperature is approximately +/- 70°K to 140°K.

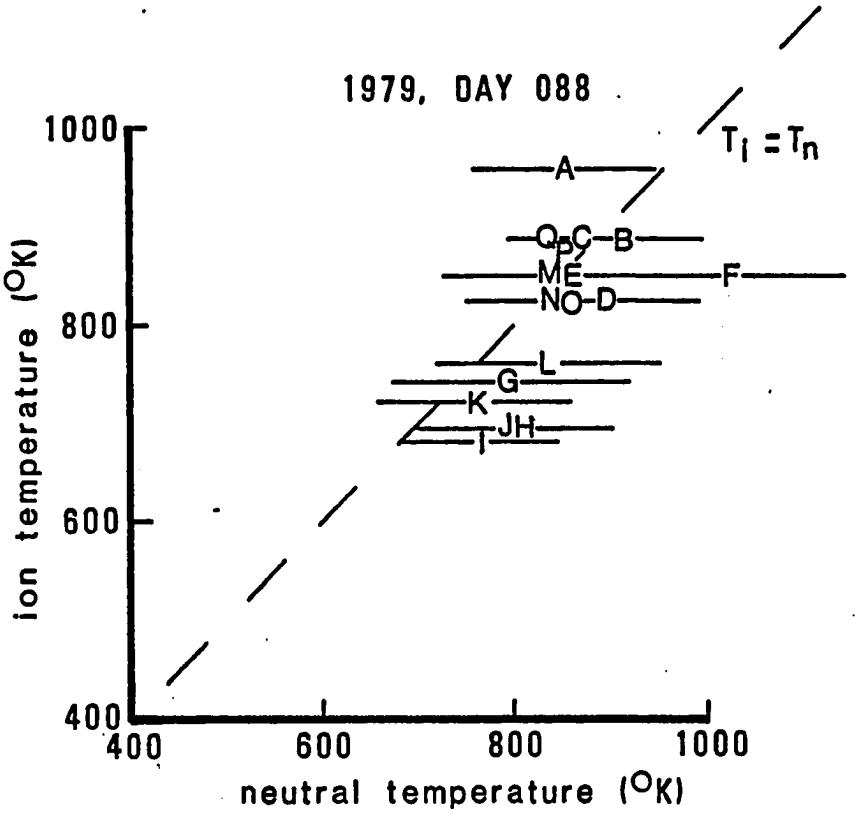

Figure 19a. Neutral vs ion temperature at 200km. Letters correspond to times indicated in Figure 16. A 100% O^+ atmospheric model is used to calculate ion temperature; uncertainty in ion temperature is approximately +/- 90^{O}K.

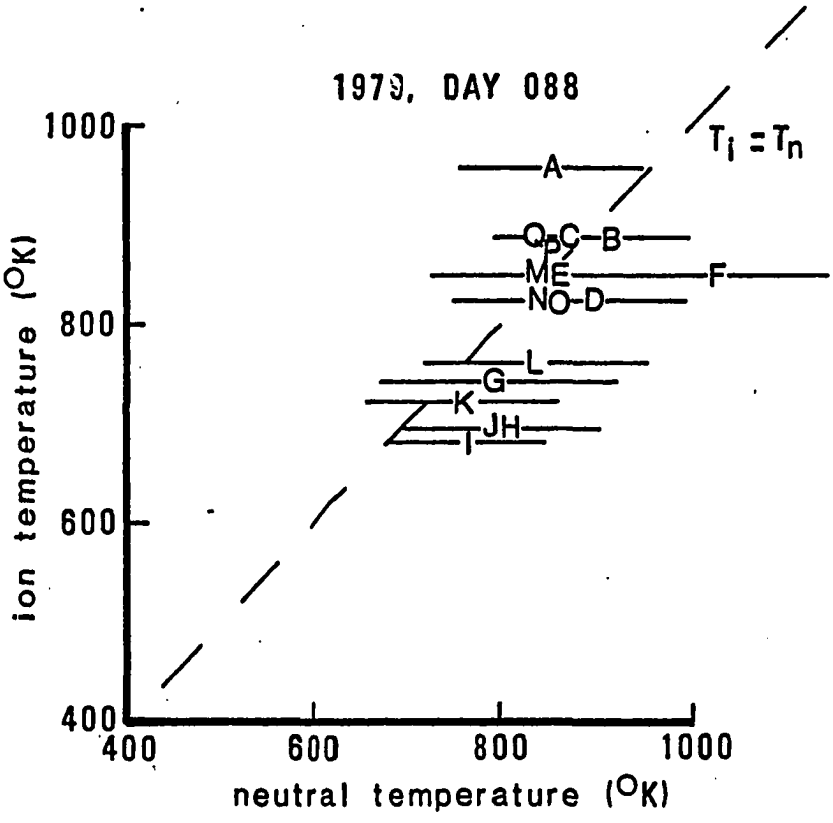

Figure 19b. Neutral vs electron temperature at 200km. Letters correspond to times indicated in Figure 16. A 100% O^+ atmospheric model is used to calculate electron temperature; uncertainty in electron temperature is approximately +/- 90°K.

altitude to above 200km. Uncertainty of measurements do not allow variations in composition to be studied in detail.

The correlation between ion and neutral temperatures in Figures 17-19 shows that the observed temperature is, in fact, the real value for neutral temperature. The co-varying relationship between 600^{o} and 1000^{o}K indicates that real and measurable temperature changes in the atmosphere do occur. A closer examination of the data may reveal why the temperature variations exist.

Ohmic heating and particle energy input, derived from equations 23 and 24 respectively, are calculated for day 052 in Figure 20. Particle energy input is calculated with an approximately 10 minute time resolution using the intensity of the 4278A emission (MSP data, equations 24 and 25) and for 35 minute intervals using electron density profiles (radar data, equations 24 and 26). Particle energy input is most significant near 0740UT and 1000UT. The heating at 1000UT may have been confined to a narrow strip and be of short duration as it is not recorded by the radar. Radar measurements for the electric field and the height-integrated Pederson conductivity yield the Ohmic energy input (equation 23) which is maximum near 0600UT. The total energy input in Figure 20 is the sum of the particle and Ohmic energies using the radar data (available for day 052 only).

For day 052, points A-D indicate substantial energy

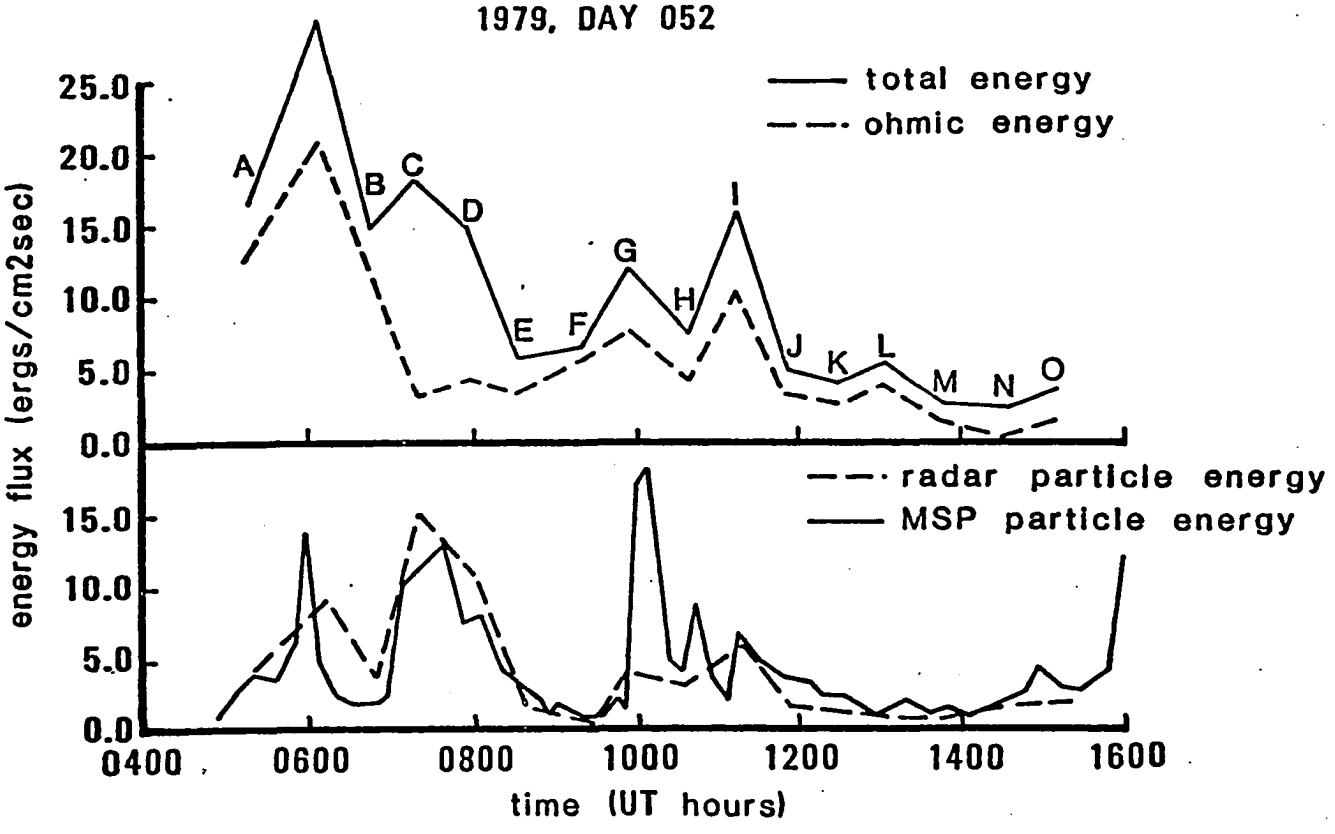

Figure 20. Auroral energy input.

input. The temperature data for these points (Figures 16 and 17) indicate that the ion temperature may be greater than the neutral temperature during heating but uncertainties in temperature measurements precluded a definite conclusion.

Atmospheric temperatures (Figure 16) decrease after auroral input has subsided. In Figure 21a the total energy flux determined by the radar is shown as a function of the neutral temperature deduced for the same time. A correlation is not evident. Thus it cannot be determined whether transient, local temperature anomalies occur as a result of auroral heating or whether the 35 minute time resolution is insufficient to resolve any heating effects.

The possibility of a phase lag between auroral energy input and an increase in neutral temperature exists. In Figure 21b, the total energy input is shown versus the neutral temperature 4 hours later. The correlation indicates that auroral energy input does affect the temperature of the neutral atmosphere which shows why both the ion and neutral temperatures in Figures 17-19 varied more than predicted from diurnal effects.

Based on midlatitude interferometric data, Hays et al. (1969) suggest a 3-hour delay between geomagnetic activity and an exospheric thermal response. Satellite drag data, responding to density changes in the exosphere, indicate a 6-hour lag following an increase in activity. Theoretical

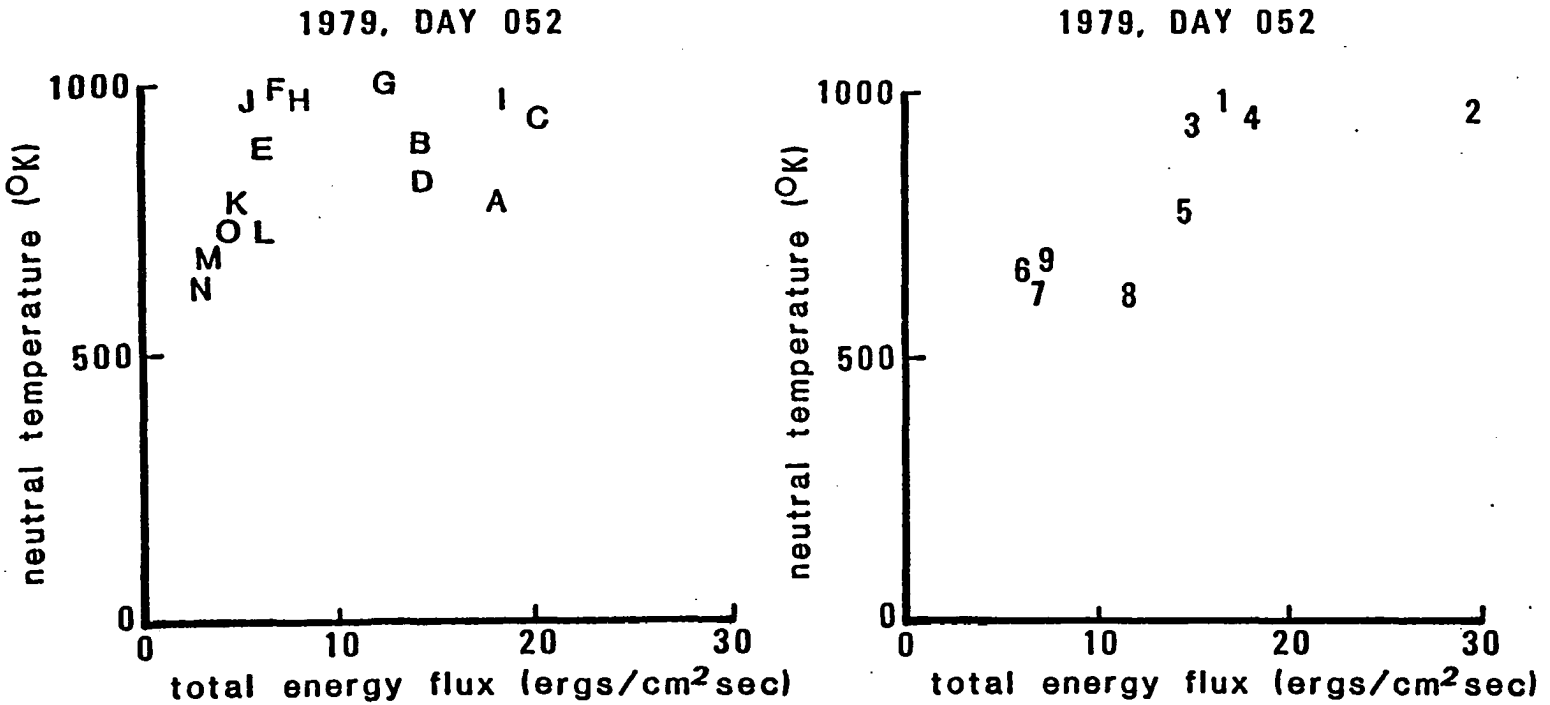

a. Energy deposition vs neutral temperature. Letters correspond to times indicated in Figure 16.

b. Energy deposition leads neutral temperature by 4 hours. Numbers correspond to sequential 4-hour intervals.

Figure 21. Neutral temperature versus auroral energy input.

studies estimate that density changes may lag thermal response by approximately 2 hours (Roble, 1969), predicting a 4-hour delay between commencement of geomagnetic activity and the midlatitude, thermal response of the exosphere. Here, the 4-hour delay appears only slightly longer than expected.

The dependence of neutral temperature on auroral energy input may be cumulative. In Figure 22, moving hourly averages of neutral temperature are shown with the Jacchia model prediction for neutral temperature at 200km. The February sequence begins with day 051 which is a day of almost no auroral activity, as shown by the magnetometer traces in Figure 23 (Townshend, 1979). Days 052-054 show more activity and correspond to a gradual increase in the average neutral temperature with respect to the Jacchia model. For days 053-054 the diurnal variation predicted by Jacchia is apparent.

The March sequence (Figures 22b and 23b) also begins with low activity and the neutral temperature follows the Jacchia predictions more closely than the February sequence. Magnetic activity increased from day 084 to day 088. For day 088 the neutral temperature was essentially equal to the Jacchia prediction.

In order to eliminate diurnal variations from the observed temperatures, the difference between the Jacchia prediction for neutral temperature (T_J) and the observed neutral temperature is compared with moving sums of the

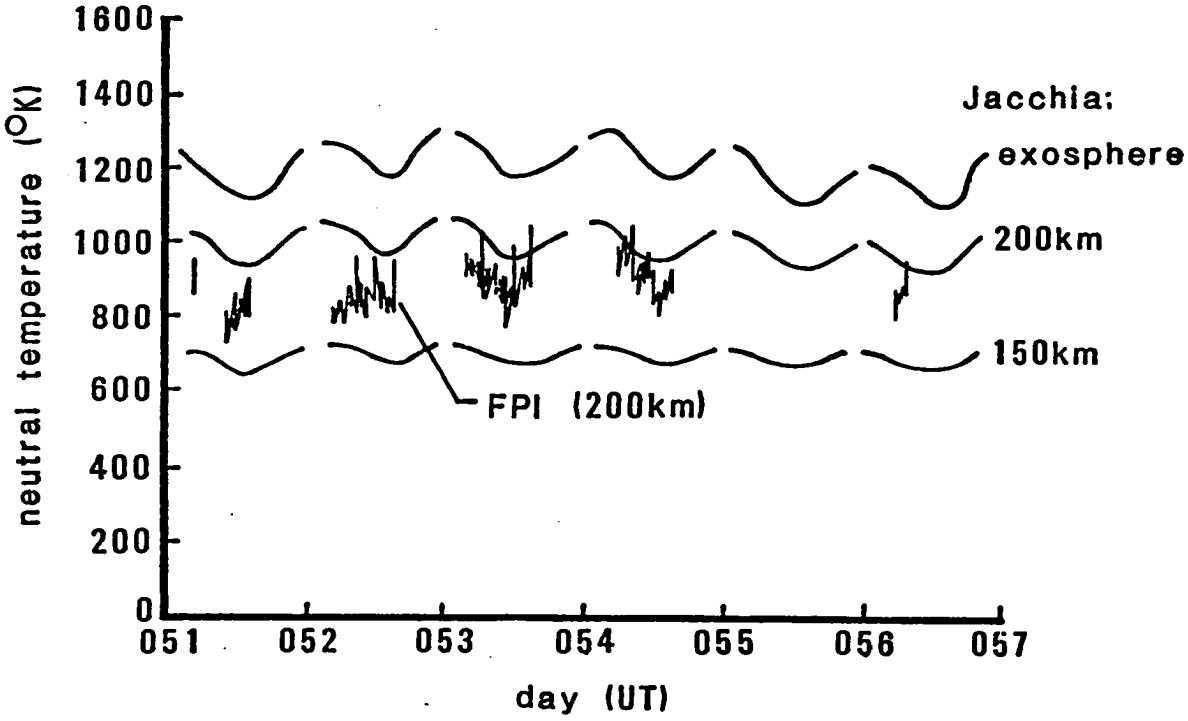

Figure 22a. Moving hourly averages of retrieved neutral temperature (adjusted for 200km) shown with the Jacchia model prediction of temperature at 150km, 200km, and exospheric during the February sequence.

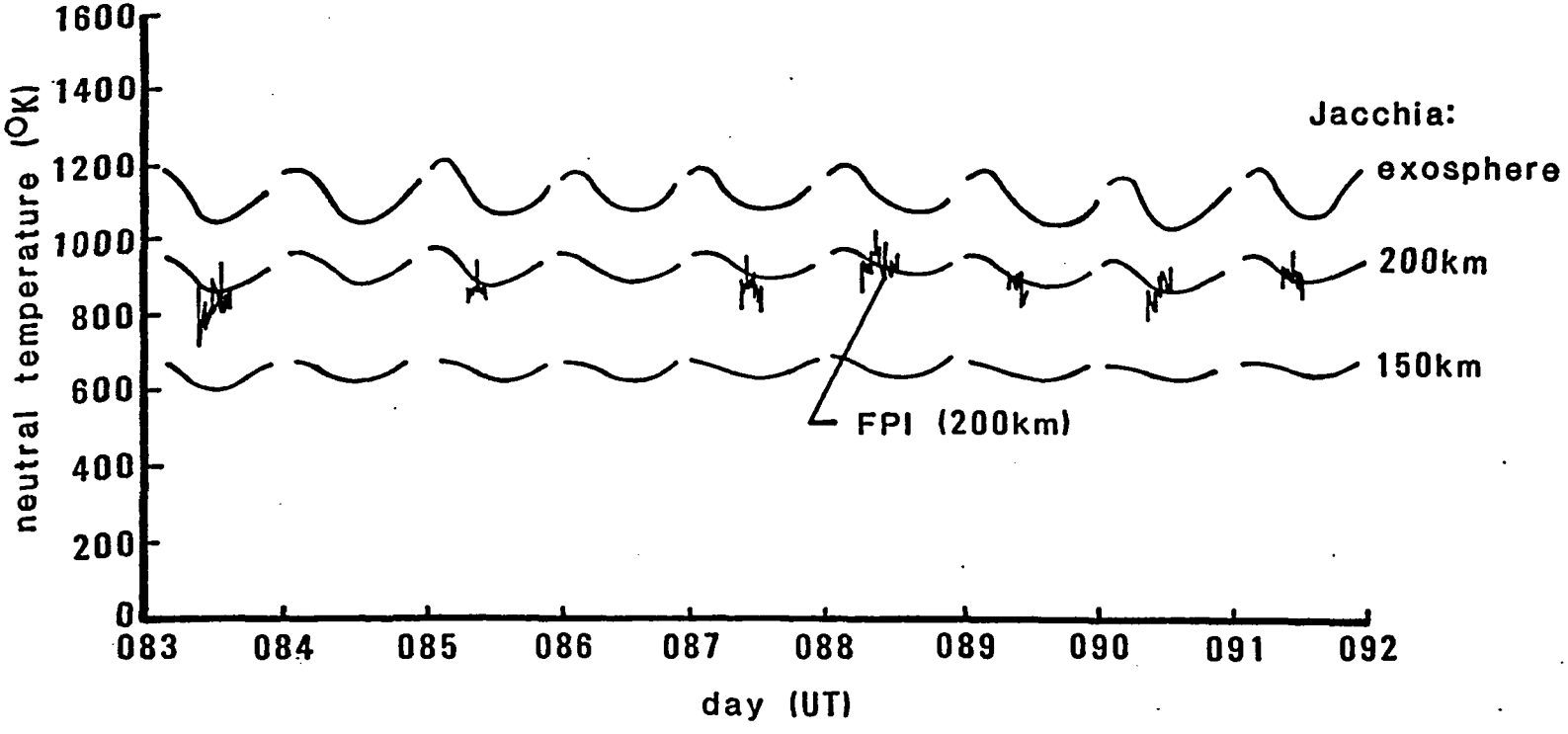

Figure 22b. Moving hourly averages of retrieved neutral temperature (adjusted for 200km) shown with the Jacchia model prediction of temperature at 150km, 200km, and exospheric during the March sequence.

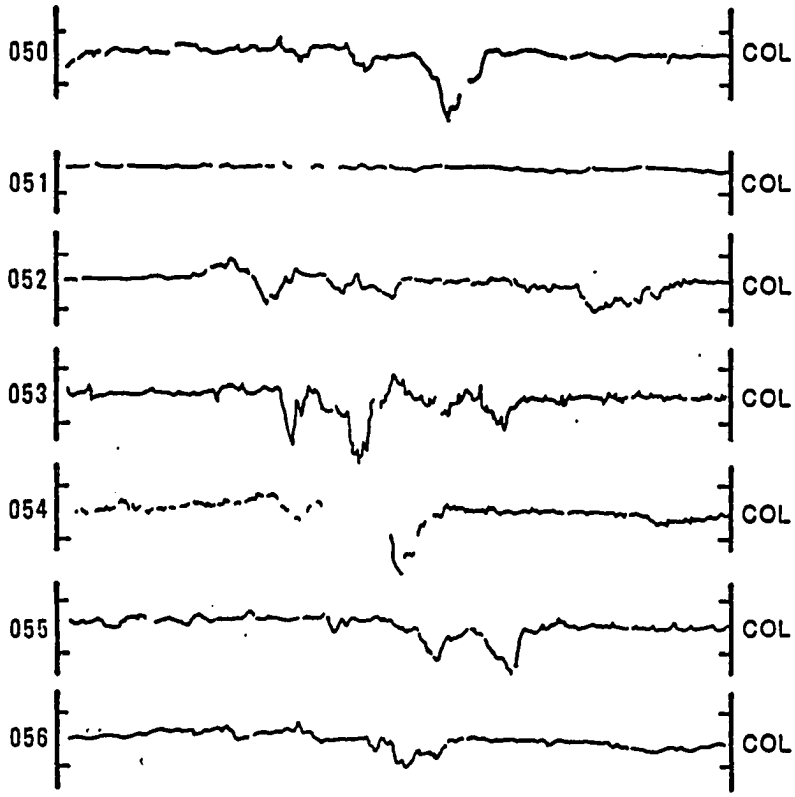

Figure 23a. Magnetometer traces for UT days 050-056. Traces are derived from the magnitude of the horizontal components of magnetic disturbance, excluding diurnal and lunar variations.

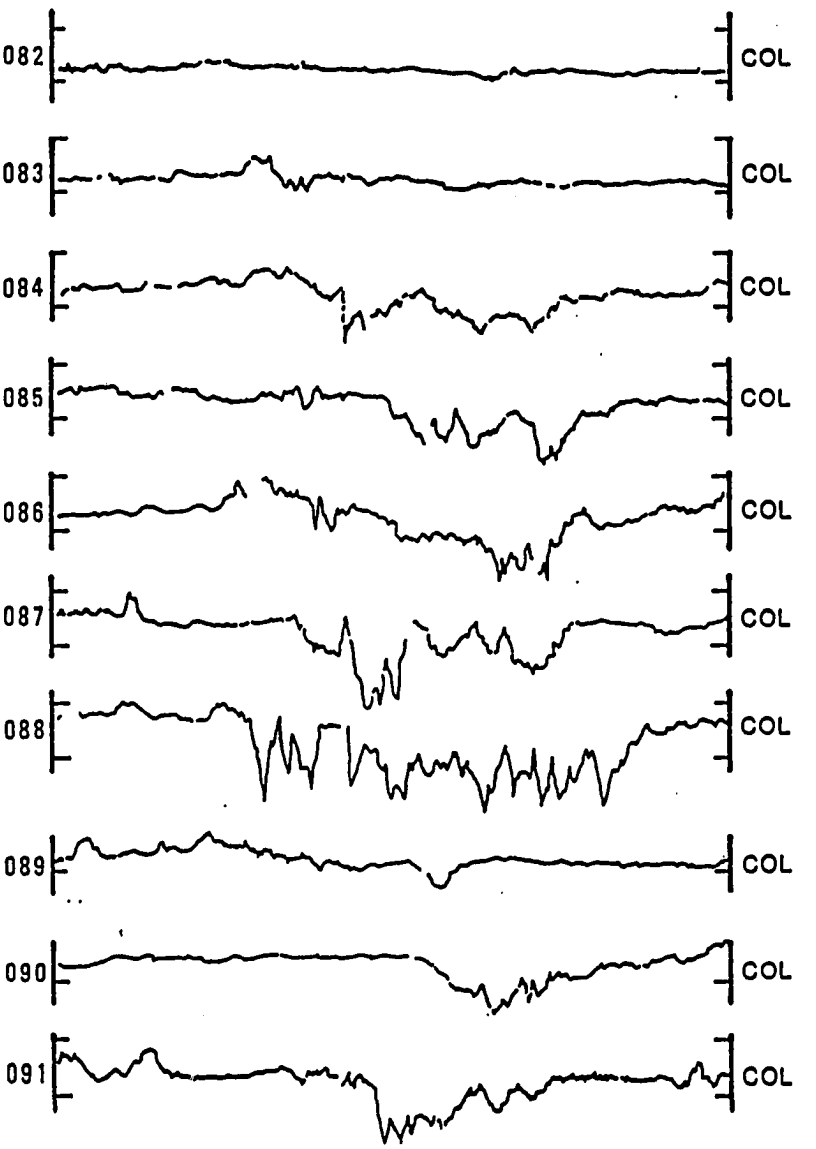

Figure 23b. Magnetometer traces for UT days 082-091. Traces are derived from the magnitude of the horizontal components of magnetic disturbance, excluding diurnal and lunar variations.

College K indices for geomagnetic activity. The temperature difference shows a fairly good correlation with the geomagnetic activity for the preceding 48-hour period (Figure 24). Thus the dependence of the neutral temperature on geomagnetic activity appears to be greater than predicted by the Jacchia model.

Jacka et al. (1979) report that the midlatitude neutral temperature in the southern hemisphere may also be more dependent on auroral activity than predicted by the Jacchia model. Their results agree with the Jacchia model for periods of little activity, but increase above the modeled values during periods of greater activity. The present data show a similar increasing trend but begin with temperature below the predicted value. The low temperature may be due to systematic errors or, alternatively, the polar atmosphere may be colder than predicted.

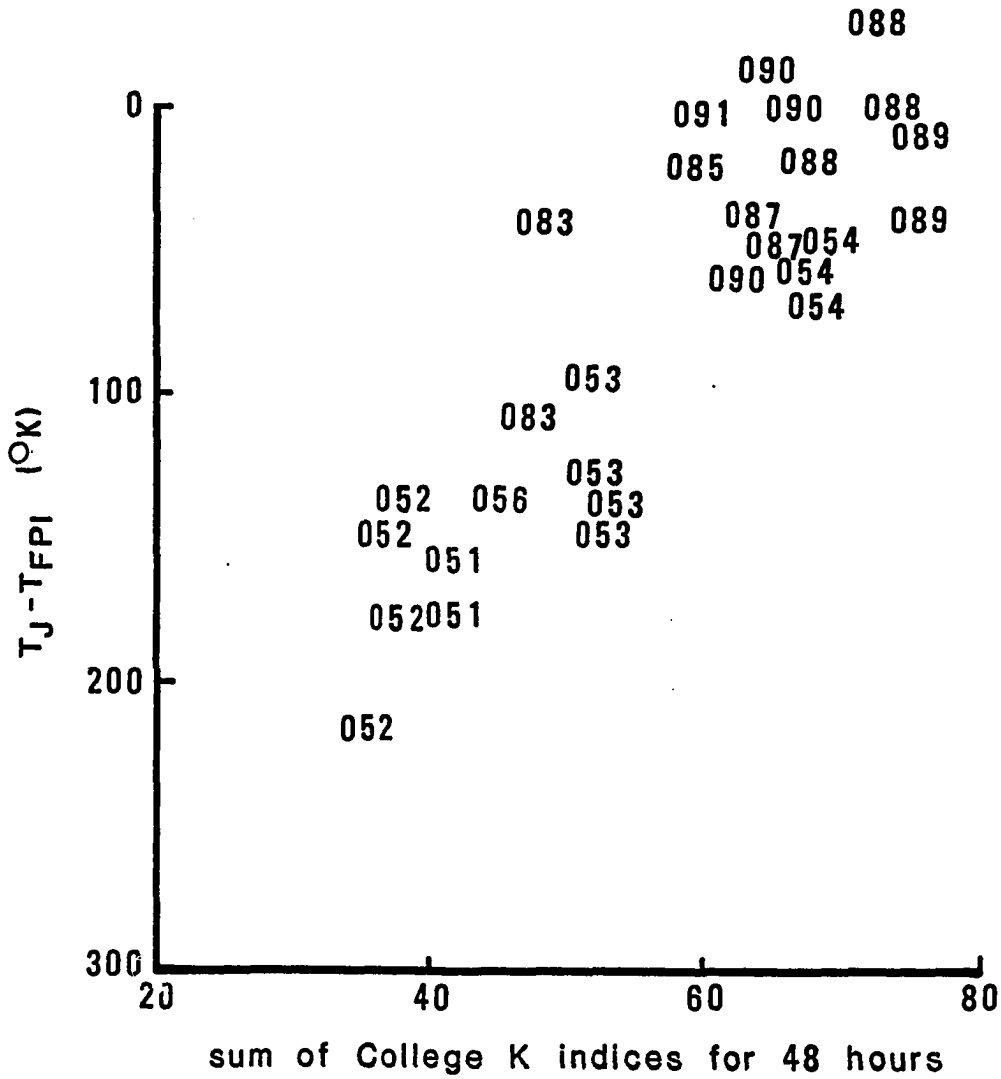

Figure 24. The difference between observed and modeled neutral temperature vs preceding 48-hour moving sum of the College K indices for the UT days indicated. Similar diagrams invoking preceding 24 and 72 hours, etc., showed more scatter.

VIII. NEUTRAL WINDS

Studies of global thermospheric winds have been synthesized by Wallis (1974) who reports primarily solar-dependent meridional winds and auroral-dependent zonal winds. Upward convection at high latitudes (predicted by Hays et al., 1973) may be associated with downward convection observed in low latitude regions during intense geomagnetic activity (Hays and Roble, 1971b). The Fabry-Perot interferometer is capable of determining winds by measuring the Doppler shift in wavelength of the radiating atom with respect to the wavelength of a stationary reference.

Several methods have been proposed for determining the Doppler shift of the fringe profiles. Gagne (1974) developed a reduction routine using weighted values of the spectral lines in coordinate space. Hays and Roble (1971b) developed a method in frequency space. The method used in this thesis is a direct application of the Fourier phase angles deduced in determining the temperature.

$$\text{Wind velocity} = \frac{\frac{c}{\cos\theta}\sum_m \left[1 - \frac{\lambda_{OBS}}{\lambda_{REF}}\right]\hat{\gamma}_m}{\sum_m \hat{\gamma}_m} \qquad (29)$$

where c = velocity of light

λ_{OBS} = observed wavelength 6300A

λ_{REF} = reference wavelength 6300A

$\Delta\lambda$ = wavelength shift = $\frac{.198}{2\pi} \times \alpha_m' \times S$

α_m' = |Fourier phase angles|

$$S = \begin{cases} +1 \text{ if } \cos(\hat{Y}_{sm}/\hat{Y}_{cm}) > 0 \\ -1 \text{ if } \cos(\hat{Y}_{sm}/\hat{Y}_{cm}) < 0 \end{cases}$$

θ = zenith angle

$\hat{Y}_m$ = Fourier coefficients

Uncertainties of measurements were approximated by a linearization procedure similar to that used in the temperature analysis. However, since the apparatus used a pressure strain gauge, allowance for possible drifts in the pressure reading were included. The measurements presented here should be regarded as preliminary.

Figure 25 comprises most of the neutral wind data for spring 1979. Generally only the meridional component of the wind was observed. However, for a few observations near local midnight, the zonal component only was observed. The results (shown together in Figure 25) are similar to those obtained by Hays et al. (1979) in January 1972 from Ester Dome. Throughout most of the night only meridional data were taken. In the evening, the meridional component of the wind vector is northward, followed by a gradual shift southward near local midnight. For the short period near local midnight when only zonal data were taken, a westward component is indicated.

Future studies may use simultaneous observations of neutral thermospheric temperature and winds to advantage.

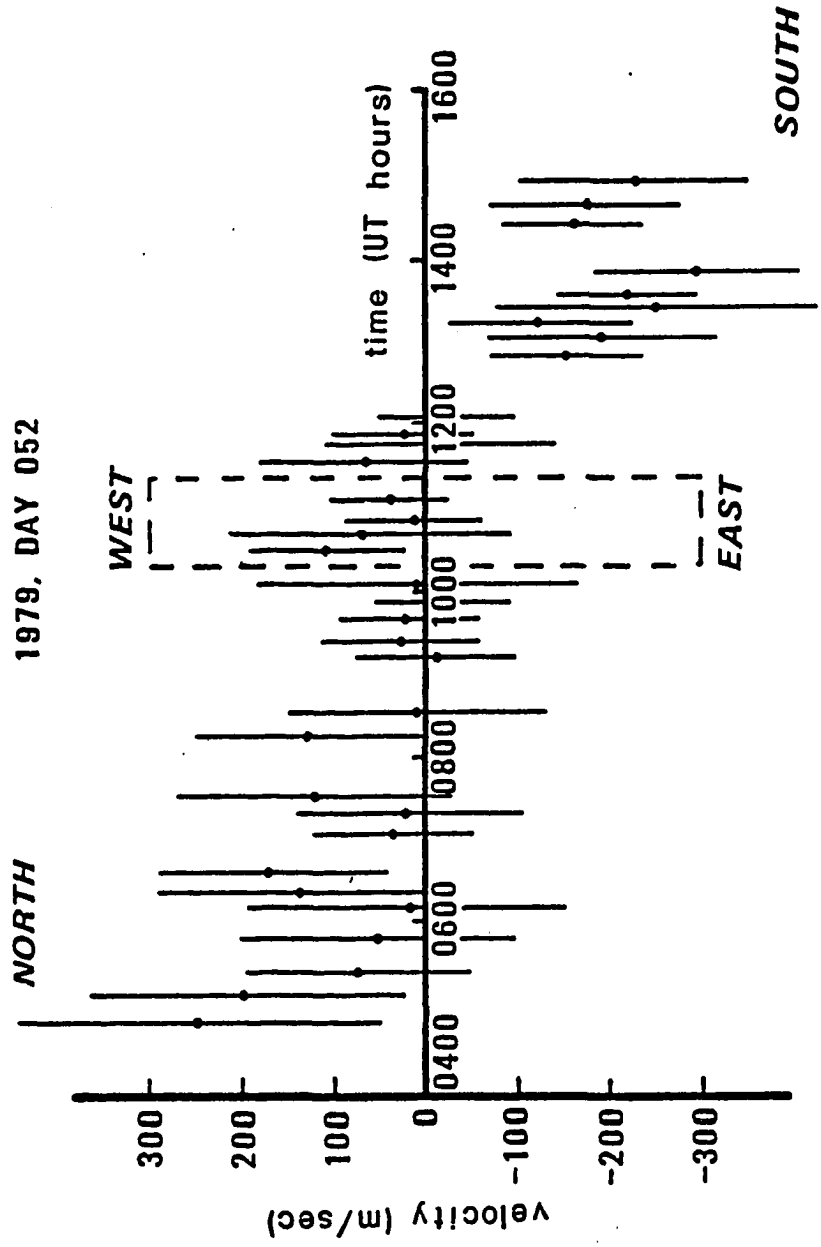

Figure 25. Neutral winds.

During the spring 1979 observations, occasional but marked fluctuations in the retrieved temperatures were noted on several nights during early morning hours. Recently Jacka et al. (1979) reported similar fluctuations observed in the 6300A airglow in the southern hemisphere and suggested that changes in wind velocities in the thermosphere may alter the retrieved temperatures.

IX. SUMMARY AND CONCLUSIONS

A pressure-scanning Fabry-Perot interferometer was installed at the Geophysical Institute's observatory located at the Poker Flat Research Range near Fairbanks, Alaska. The interferometer was capable of measuring the Doppler width of the 6300A emission line in the auroral spectrum with sufficient resolution to determine the neutral temperature and winds.

The FPI data were made compatible with the data format of an existing minicomputer system controlling meridian scanning photometers. Thus, digital data were stored on magnetic tapes.

The algorithm for numerical reduction of the data provided for a least squares matching of the observed profile with a theoretically computed profile. The theoretical profile was the convolution of both physical and instrumental broadening functions. The temperature and uncertainty of measurement were determined by iteration.

The 6300A emission originates from a range of altitudes and has different emission profiles, depending on the energy of the incident particle flux. An atmospheric model was used to predict the emission profiles for the 6300A and 4278A emissions for several auroral characteristic electron energies. Subsequently, the observed intensities

of these emissions (Meridian Scanning Photometer data) were used to predict the mean altitude of the 6300A emission and the line broadening due to temperature averaging associated with column emission effects. The neutral temperature was then deduced from the FPI data.

For several nights the average lapse rate observed for the neutral atmosphere near 200km was comparable to the lapse rate predicted by the atmospheric models of Jacchia and MSIS. Although the observed temperature was lower than the model predictions, the techniques for altitude and temperature determination appear justified. The lapse rate from the Jacchia model was used to adjust the neutral temperature to a common altitude of 200km. Deviations from the average lapse rate may indicate real local warming.

The above discussion summarizes the techniques used in determining the neutral temperature in the auroral thermosphere. The atmospheric models of Jacchia and data from the Chatanika Incoherent Scatter Radar and the College K indices, indicating local geomagnetic activity, were compared with the observed neutral temperature.

The neutral temperature generally was observed to be equal to the ion temperature and equal to or less than the electron temperature. The experimental determination of these expected relationships further justifies the analysis techniques. The covarying relationship between ion and neutral temperatures indicates that real

changes in the atmospheric temperature occur. The magnitude of the variation suggests that auroral energy input might be an important influence in determining the thermospheric temperature. Observed ion temperature may have been greater than the neutral temperature during a period of auroral energy input, but the error bars of the measurements make this conclusion uncertain.

The time resolution of the interferometric and radar observations was insufficient to determine whether auroral energy input creates significant, short-term, local temperature anomalies in the neutral atmosphere. However, a 4-hour phase lag between auroral heating and an increase in neutral temperature was evident. Thus, the temperature of the polar atmosphere appears dependent on the amount of auroral energy input.

The possible cumulative effect on the aurora was then examined. The difference between observed temperature and the Jacchia prediction correlated well with a 2-day sum of the K index for local geomagnetic activity. These conclusions imply that the temperature of the thermosphere is more dependent on auroral energy input than is predicted by the Jacchia model.

REFERENCES

Babcock, H. D., "A Study of the Green Auroral Line by the Interference Method", Astrophysical Journal, 57, 209, 1923.

Ballik, E. A., "The Response of Scanning Fabry-Perot Interferometers to Atomic Transition Profiles", Applied Optics, 5, 170, 1966.

Born, M. and E. Wolf, Principles of Optics, Pergamon Press, NY, 1959.

Chabbal, R., J. Rech. Centre Nat. Rech. Sci. Lab., Bellevue, Paris, 24, 138, 1953.

Cocks, T. D. and F. Jacka, "Daytime Thermospheric Temperatures, Wind Velocities and Emission Intensities Derived from Ground Based Observations of the OI 630nm Airglow Line Profile", Journal of Atmospheric and Terrestrial Physics, 41, 409, 1979.

Chamberlain, J. W., Physics of the Aurora and Airglow, Academic Press, Inc., NY, 1961.

Gagne, J-M., J-P. Saint-Dizier, et M. Picard, "Methode d'echtillonnage des fonctions deterministes en spectroscopie: application a un spectrometre multicanal par comptage photonique", Applied Optics, 13, 581, 1974.

Hays, P. B., A. F. Nagy, and R. G. Roble, "Interferometric Measurements of the 6300A Doppler Temperature During a Magnetic Storm", Journal of Geophysical Research, 74, 4162, 1969.

Hays, P. B. and R. G. Roble, "A Technique for Recovering Doppler Line Profiles from Fabry-Perot Interferometric Fringes of Very Low Intensity", Applied Optics, 10, 193, 1971a.

Hays, P. B. and R. G. Roble, "Direct Observation of Thermospheric Winds During Geomagnetic Storms", Journal of Geophysical Research, 76, 5316, 1971b.

Hays, P. B., R. A. Jones, and M. H. Rees, "Auroral Heating and Composition of the Neutral Atmosphere", Planetary and Space Sciences, 21, 559, 1973.

Hays, P. B., D. W. Rusch, R. G. Roble, and J. C. G. Walker, "The OI (6300A) Airglow", Reviews of Geophysics and Space Physics, 16, 225, 1978.

Hays, P. B., J. W. Meriwether, and R. G. Roble, "Nighttime Theromspheric Winds at High Latitudes", Journal of Geophysical Research, 84, 1905, 1979.

Hedin, A. E., Table of Thermospheric Temperature, Density, and Composition Derived from Satellite and Ground Based Measurements, NASA/Goddard Space Flight Center, MD, 1979.

Hernandez, G. and R. G. Roble, "Thermospheric Dynamics Invesigations with Very High Resolution Spectrometers", Applied Optics, 18, 3376, 1979.

Jacchia, L. G., "Static Diffusion Models of the Upper Atmosphere with Empirical Temperature Profiles", Smithsonian Contributions to Astrophysics, 8, 215, 1965.

Jacka, F., A. R. Bower, and P. A. Wilksch, "Thermospheric Temperatures and Winds Derived from OI 630nm Night Airglow Line Profiles", Journal of Atmospheric and Terrestrial Physics, 41, 397, 1979.

Kelly, J. D., "Radar Measurements of Temperatures and Ionic Composition in the High-Latitude Ionosphere", University of Alaska, dissertation, 1979.

Knudson, J. R., D. C. Kayser, and W. E. Potter, "Mass Spectrometer Measurement of Thermospheric Winds", Journal of Geophysical Research, 82, 5353, 1977.

Nilson, J. A. and G. G. Shephard, "Upper Atmospheric Temperature from Doppler Line Widths I: Some Preliminary Measurments of OI 5577A Aurora", Planetary Space Science, 5, 299, 1961.

Nussbaum, A. and R. A. Phillips, Contemporary Optics for Scientists and Engineers, Prentice-Hall, Inc., NJ, 1976.

Rees, M. H. and D. Luckey, "Auroral Electron Energy Derived from Ratio of Spectroscopic Emissions I: Model Computation", Journal of Geophysical Research, 79, 5181, 1974.

Richmond, A. D., "Thermospheric Heating in a Magnetic Storm: Dynamic Transport of Energy from High to Low Latitudes", Journal of Geophysical Research, 84, 5259, 1979.

Roble, R. G., "A Theoretical and Experimental Study of the Stable Mid-latitude Red Arc (SAR-ARC)", University of Michigan, dissertation, 1969.

Romick, G. J., "The Detection and Study of the Visible Spectrum of the Aurora and Airglow", Methods for Atmospheric Radiometry, 91, 63, 1976.

Rusch, D. W., J-C. Gerard and W. E. Sharp, "The Reaction of $N(^2D)$ with O_2 as a Source of $O(^1D)$ Atoms in Aurorae", Geophysical Research Letters, 5, 1043, 1978.

Shore, B. W. and D. H. Mentzel, Principles of Atomic Spectra, John Wiley and Sons, Inc., NY, 1968.

Townshend, J. B., ed., "Preliminary Geomagnetic Data, College Observatory, Fairbanks, Alaska", United States Department of the Interior, Geological Survey, 79-300, 1979.

Vallance-Jones, A., Aurora, D. Reidel Publishing Company, MA, 1974.

Wallis, D. D., "Geomagnetic Influences on Thermospheric Winds Observed in the Auroral Zone", University of Alaska, dissertation, 1974.

Wickwar, V. B., "Analysis Techniques for Incoherent-Scatter Data Interpretation in the 100-300km Region", Technical Report 3, Contract DNA001-72-C-0076, Stanford Research Institute, CA.

APPENDIX

Following is a schematic diagram of the interface that makes the Fabry-Perot interferometric data compatible with the Meridian Scanning Photometer system. Data are stored on magnetic tape and are then available for digital processing, as described in the text.

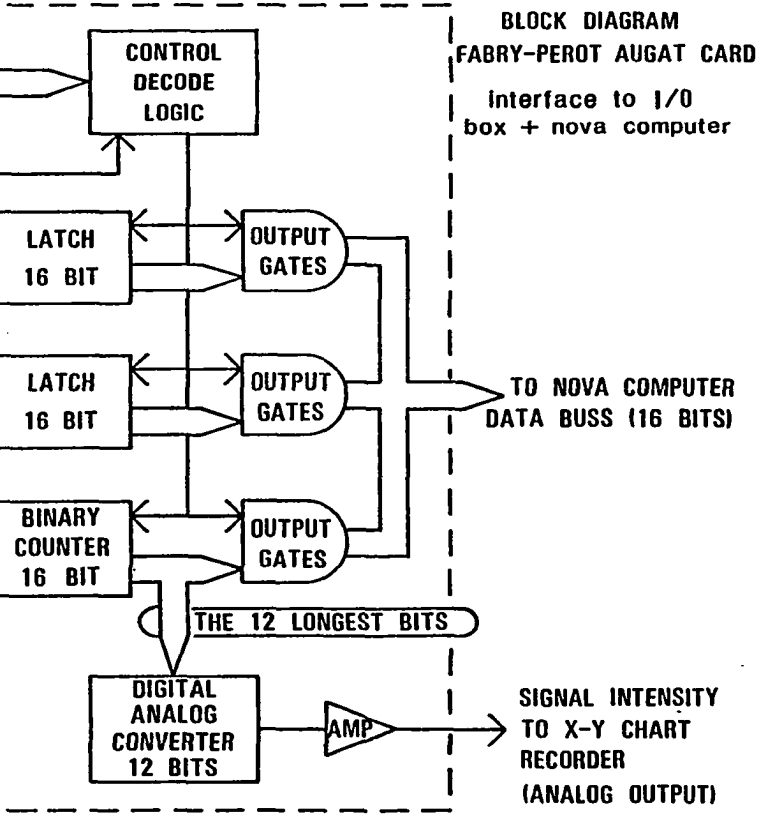
BLOCK DIAGRAM
FABRY-PEROT AUGAT CARD
Interface to I/O
box + nova computer
CONTROL
DECODE
LOGIC
LATCH
16 BIT
OUTPUT
GATES
LATCH
16 BIT
OUTPUT
GATES
TO NOVA COMPUTER
DATA BUSS (16 BITS)
BINARY
COUNTER
16 BIT
OUTPUT
GATES
THE 12 LONGEST BITS
DIGITAL
ANALOG
CONVERTER
12 BITS
AMP
SIGNAL INTENSITY
TO X-Y CHART
RECORDER
(ANALOG OUTPUT)

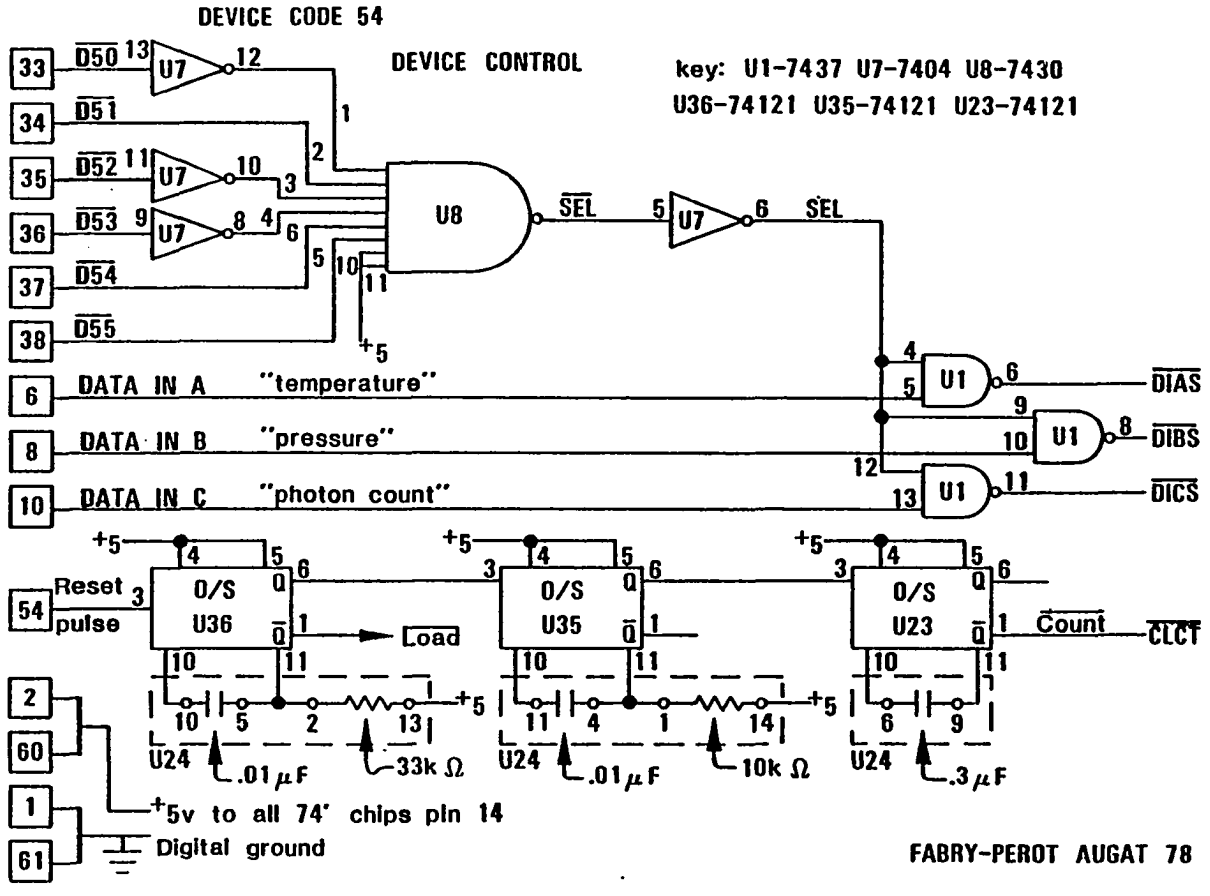

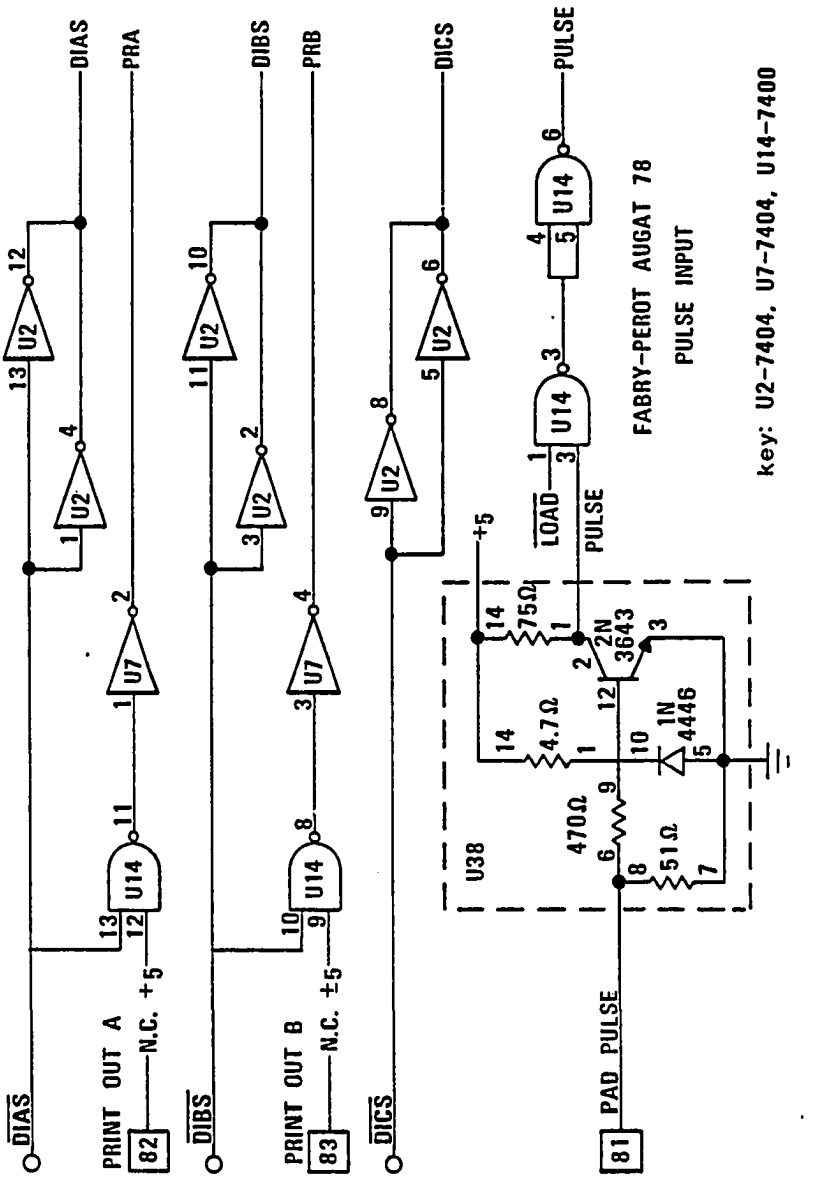

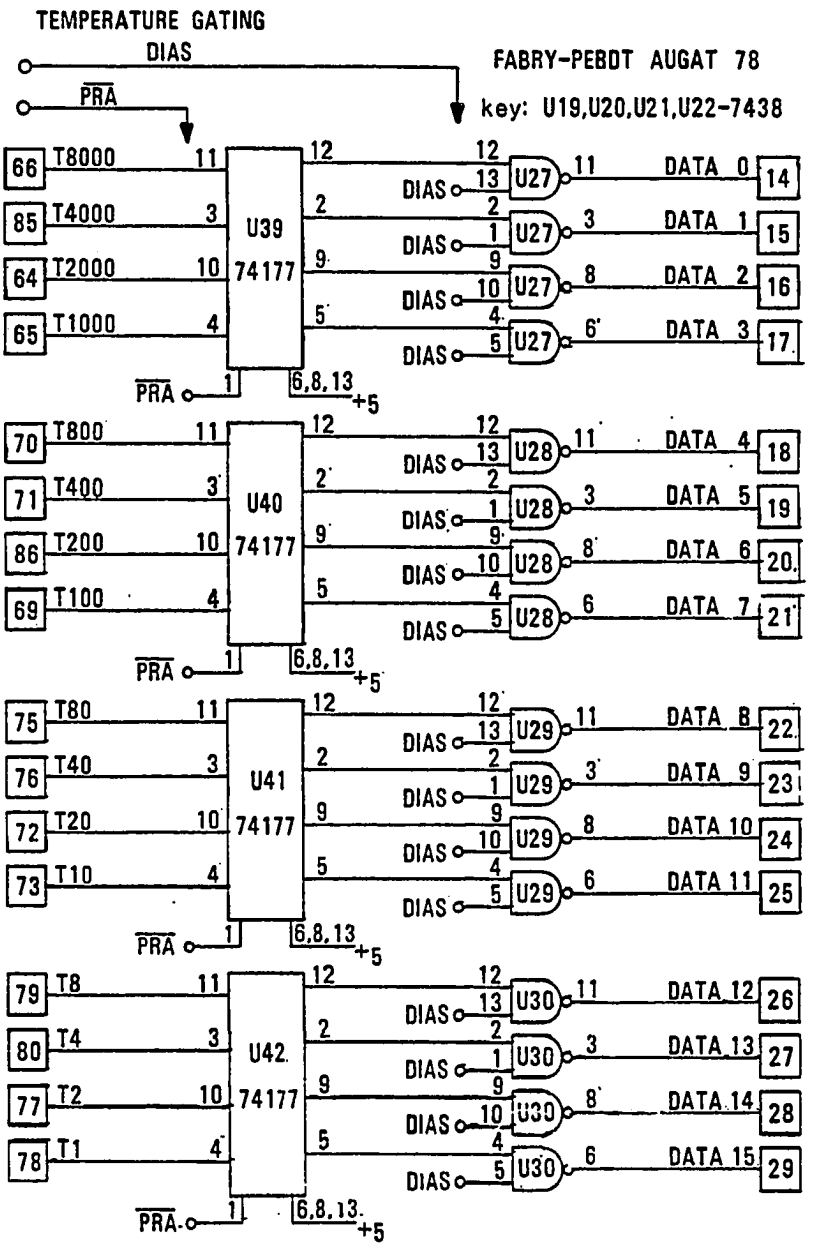

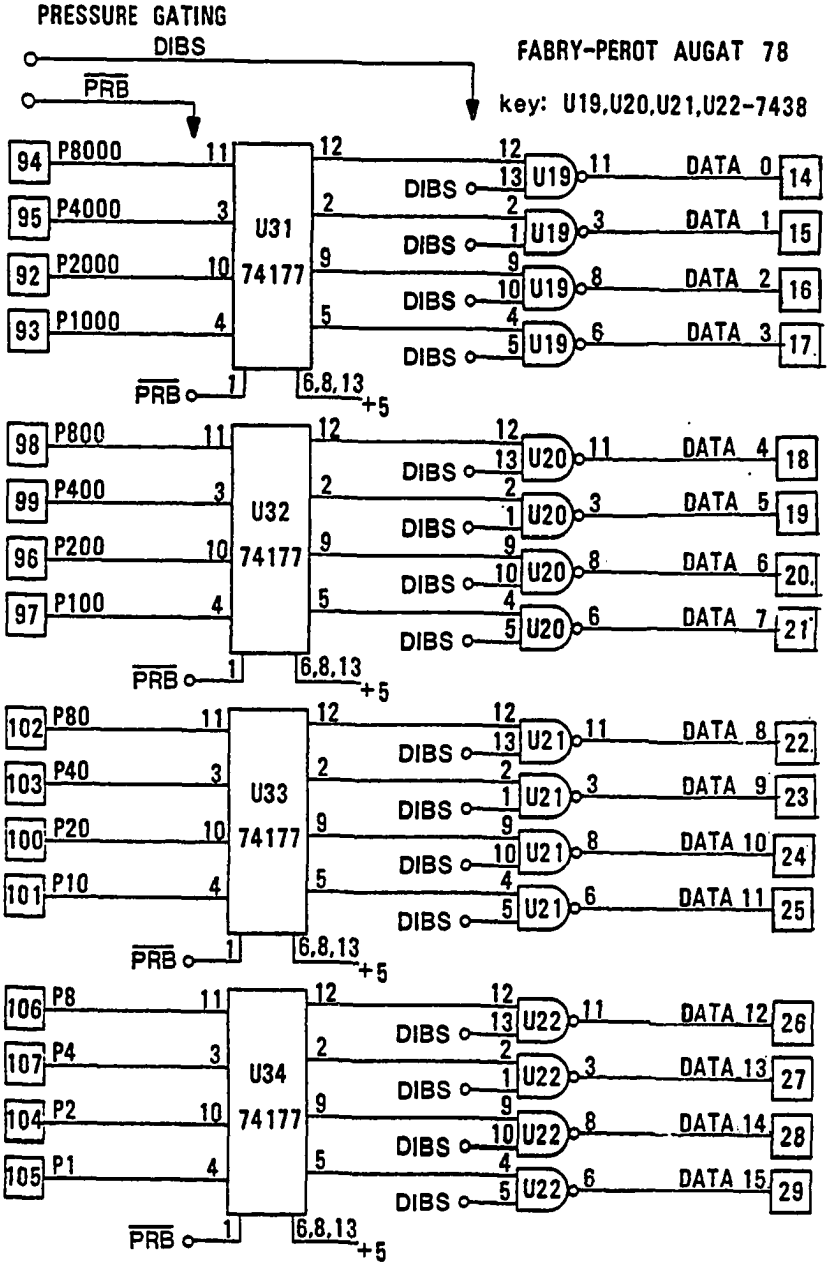

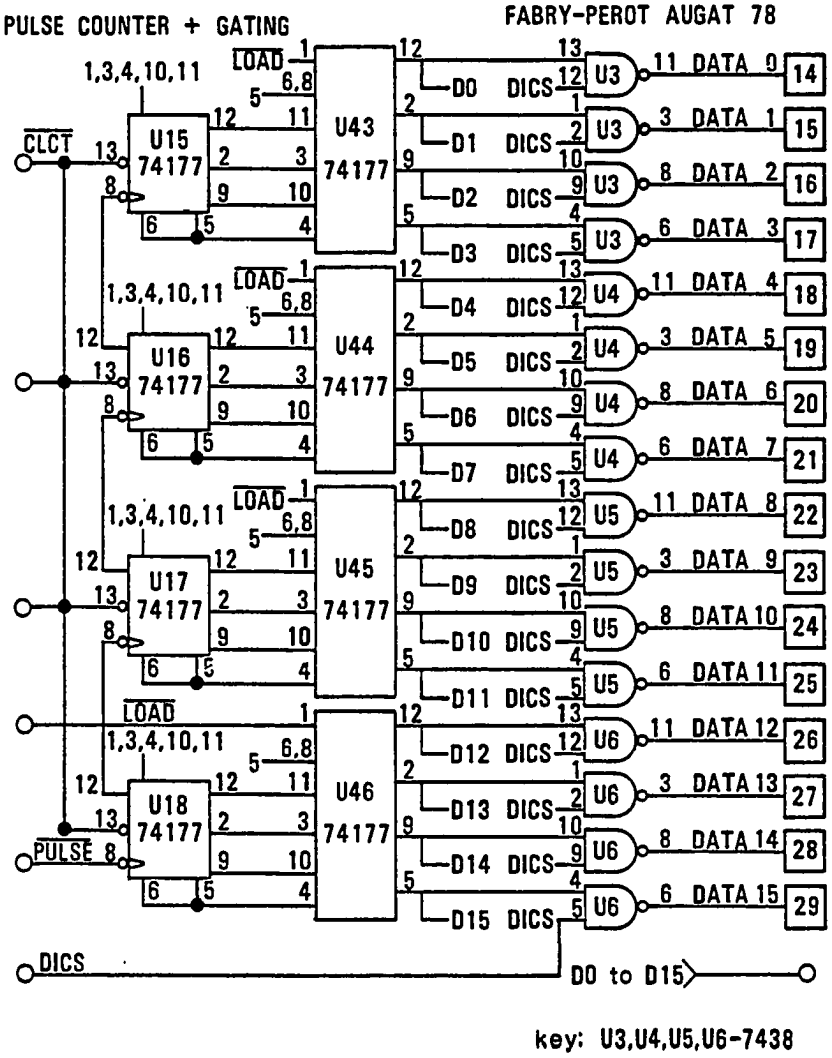

key: U3,U4,U5,U6-7438

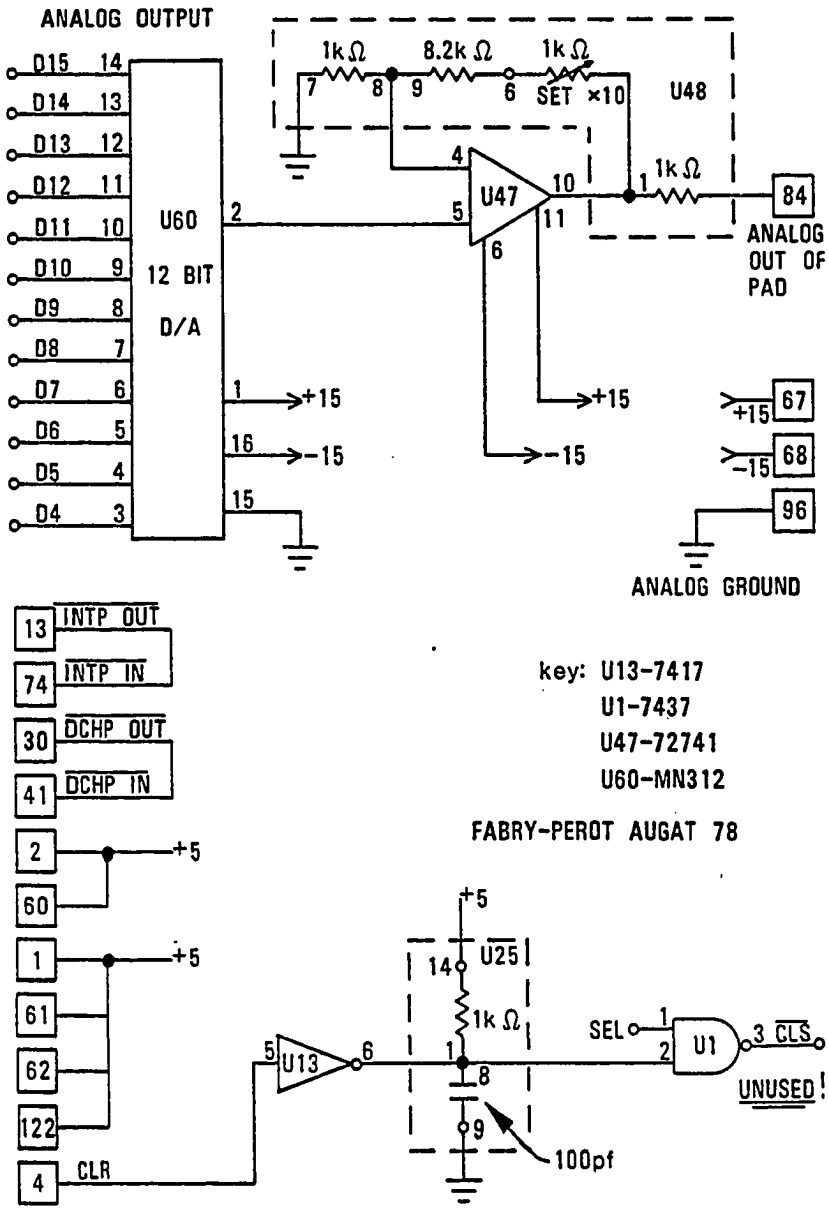

BACK VIEW of BACK PLANE CONNECTOR CARD: FABRY-PEROT
INCLUDING INTERFACE CONNECTIONS

SIGNAL	PIN NO.		SIGNAL	NOTE
GND	1	62	GND	
+5 V	2	63	-5 V	
START	3	64	T2000	temperature
CLEAR	4	65	T1000	
IO PULSE	5	66	T8000	
DATA IN A	6	67	+15 V	
DATA OUT A	7	68	-15 V	
DATA IN B	8	69	T100	
DATA OUT B	9	70	T800	
DATA IN C	10	71	T400	
DATA OUT C	11	72	T20	
IO RESET	12	73	T10	
$\overline{\text{INTP OUT}}$	13	74	$\overline{\text{INTP IN}}$	
$\overline{\text{DATA 0}}$	14	75	T80	
$\overline{\text{DATA 1}}$	15	76	T40	
$\overline{\text{DATA 2}}$	16	77	T2	
$\overline{\text{DATA 3}}$	17	78	T1	
$\overline{\text{DATA 4}}$	18	79	T8	
$\overline{\text{DATA 5}}$	19	80	T4	
$\overline{\text{DATA 6}}$	20	81	PAD	photometer pulses
$\overline{\text{DATA 7}}$	21	82	PRINT OUT A	temperature
$\overline{\text{DATA 8}}$	22	83	PRINT OUT B	pressure
$\overline{\text{DATA 9}}$	23	84	ANALOG OUT	signal intensity
$\overline{\text{DATA 10}}$	24	85	T4000	
$\overline{\text{DATA 11}}$	25	86	T200	
$\overline{\text{DATA 12}}$	26	87		
$\overline{\text{DATA 13}}$	27	88		
$\overline{\text{DATA 14}}$	28	89		
$\overline{\text{DATA 15}}$	29	90	GND	
$\overline{\text{DCHP OUT}}$	30	91	$\overline{\text{DCHP IN}}$	
MSKO	31	92	P2000	pressure
INTACK	32	93	P1000	

SIGNAL	PIN NO.		SIGNAL	NOTE
$\overline{DS\ 0}$	33	94	P8000	
$\overline{DS\ 1}$	34	95	P4000	
$\overline{DS\ 2}$	35	96	P200	
$\overline{DS\ 3}$	36	97	P100	
$\overline{DS\ 4}$	37	98	P800	
$\overline{DS\ 5}$	38	99	P400	
$\overline{INTR}$	39	100	P20	
RQENB	40	101	P10	
$\overline{DCHR}$	41	102	P80	
$\overline{SELO}$	42	103	P40	
$\overline{SELB}$	43	104	P2	
DCHA	44	105	P1	
$\overline{DCHM0}$	45	106	P8	
$\overline{DCHM1}$	46	107	P4	
DCHO	47	108		
DCHI	48	109		
OURFLO	49	110		
	50	111		
	51	112		
	52	113		
	53	114		
	54	115		
	55	116		
	56	117		
	57	118		
	58	119		
	59	120		
+5	60	121	+5	
GND	61	122	GND	

No mask
Device code 054
CLR no function
Start no function
Pulse no function

Data format: 16 bits
DIA = temperature = BCD
DIB = pressure = BCD
DIC = counts = binary

INPUT/OUTPUT CONNECTIONS CARD: FABRY-PEROT

TEMPERATURE VOLTMETER	PANEL	FUNCTION	I/O BOX	HARMONICA PLUG
B	20	T1	35	78
A	19	T2	36	77
D	18	T4	37	80
C	17	T8	38	79
2	16	T10	39	73
1	15	T20	40	72
4	14	T40	41	76
3	13	T80	42	75
F	12	T100	43	69
E	11	T200	44	86
J	10	T400	45	71
H	9	T800	46	70
G	8	T1000	47	65
5	7	T2000	48	64
8	6	T4000	49	85
7	5	T8000	50	66
*	21	PRINT	34	82

PRESSURE VOLTMETER	PANEL	FUNCTION	I/O BOX	HARMONICA PLUG
B	11	P1	1	105
A	12	P2	2	104
D	36	P4	3	107
C	37	P8	4	106
2	13	P10	5	101
1	14	P20	6	100
4	38	P40	7	103
3	39	P80	8	102
F	15	P100	9	97
E	16	P200	10	96
J	40	P400	11	99
H	41	P800	12	98
6	17	P1000	13	93
5	18	P2000	14	92
8	42	P4000	15	95
7	43	P8000	16	94
*	49	PRINT	17	93

MISCELLANEOUS	FUNCTION	I/O BOX	HARMONICA
PAD	BNC connector; pulse	25	81
GND		18	1,61
X-Y CHART	Analog out	33	84

*unused